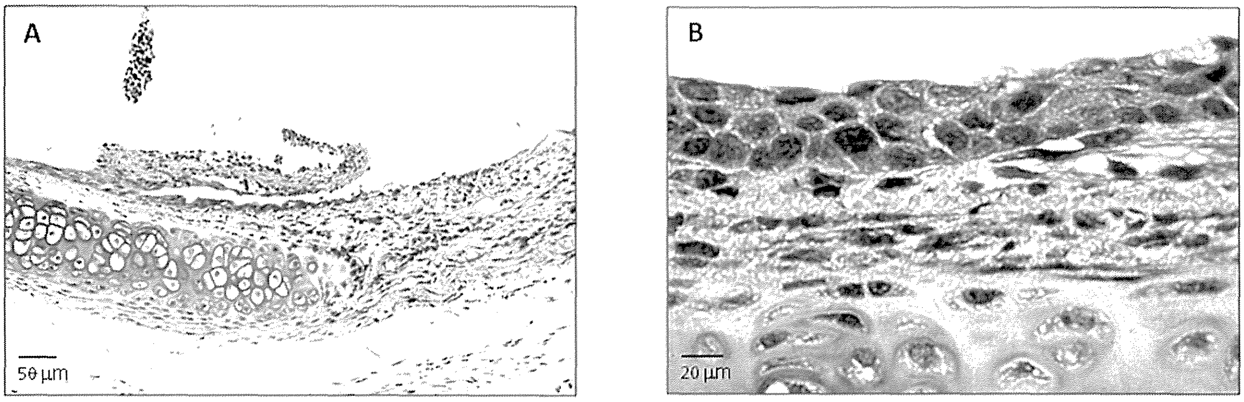

Fig. 2. Erosive lesions and squamous cell metaplasia. A, Representative image showing erosive lesions induced by treatment of MWCNT-L or MWCNT-S; B, Representative image of squamous cell metaplsia.

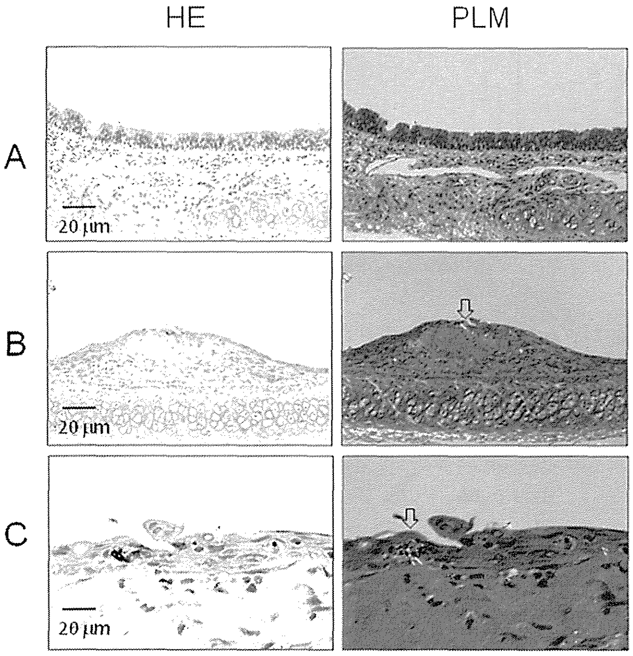

Fig. 3. Tracheal lesions in rat treated with MWCNT-L. A, Undamaged tracheal ciliated epithelium; B, An erosive lesion with granulation tissue underneath the thin regenerating epithelium; C, A higher magnification image of the lesion in B. MWCNT-L fibers (open arrows) can be clearly observed in the granulation tissue by polarized light microscopy (PLM).

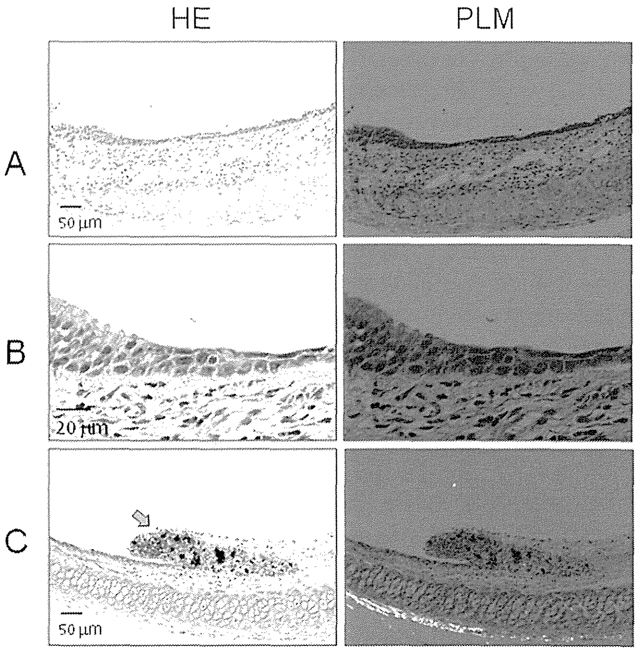

Fig. 4. Tracheal lesions in a rat treated with MWCNT-S. A, Tracheal epithelium showing a transition from undamaged ciliated epithelium to regenerating flat epithelium overlying edematous granulation tissue. B, A higher magnification image of the lesion in B. C, An erosive lesion with granulation tissue containing many black MWCNT-S fibers. MWCNT-S fibers are not visualized by polarized light microscopy (PLM).

posed of a single layer of columnar ciliated cells. Treatment with MWCNT-L induced marked damage to the surface ciliated cells resulting in erosive changes (Fig. 2A) and replacement with flat cells without cilia and occasional squamous cell metaplasia (Fig. 2B). An increase in goblet cells was found in the columnar ciliated cell area, although goblet cell damage was not obvious. MWCNT-L fiber aggregates were frequently observed in the lesions (Figs. 3B and 3C) but not in the healthy mucosa (Fig. 3A). MWCNT-S caused similar mucosal damage (Fig. 4,

Table 1. Lesions in the tracheal epithelium and lung

Treatment	No. of rats	Tracheal epithelium			Lung
		Erosion	Regenerated cells		Granulation tissue (No./cm^2) ^{b}
		Incidence (%)	Incidence (%)	Proportion ^{a} (%)	
Vehicle	4	0	0	0	0
MWCNT-L	3	100 ***	100 ***	27.2 ± 8.7**	0.1 ± 0.1
MWCNT-S	4	25 ***	100 ***	32.7 ± 11.5**	1.0 ± 0.2 **,$^{\#\#}$

Notes: ^{a}, the length of the regenerated lesion compared to the total length of the transverse tracheal circle; ^{b}, the number of granulation lesions per square centimeter of the lung tissue; ** and *** represent *p* values < 0.01 and 0.001, vs the vehicle; $^{\#\#}$ represents *p* values < 0.01, vs MWCNT-L

left panel) but, because of lack of MWCNT-S mediated polarization, the fibers could not be detected by polarized light microscopy (Fig. 4C, right panel).

Table 1 shows the incidences of erosion and incidences and the percentage of the length of the tracheal lesions compared to the total length of the tracheal cross section from rats administered vehicle or MWCNT. Tracheal lesions in rats administered MWCNT-L (27.2 ± 10.5) or MWCNT-S (32.1 ± 15.8) were significantly greater than in rats administered vehicle alone ($p < 0.001$ for both comparisons). Although not significant, the incidences of erosive lesions for MWCNT-L administered rats was greater than for MWCNT-S administered rats.

The ratio of fluorescence of acetyled tublin on the surface of the trachea (0.48 ± 0.06) to submucosal DAPI fluorescence significantly decreased ($p < 0.05$) in rats treated with MWCNT-L (Fig. 5). The value for the MWCNT-S treated rats showed a similar decrease but was not significant. The results clearly indicate the quantitative loss of ciliated cells by treatment with MWCNT-L.

In the lung, granulation foci composed of macrophages and fibrotic cells surrounding MWCNT aggregates was found (Fig. 6). Table 1 shows the number of granulation foci in the lungs of rats administered vehicle or MWCNT. The number of lesions in both the MWCNT-L and MWCNT-S administered groups were significantly higher than in the vehicle control group ($p < 0.001$ for both comparisons). The lesion count in the MWCNT-S group (1.04 ± 0.18) was significantly greater than the MWCNT-L group (0.06 ± 0.06) ($p < 0.05$) (Table 1).

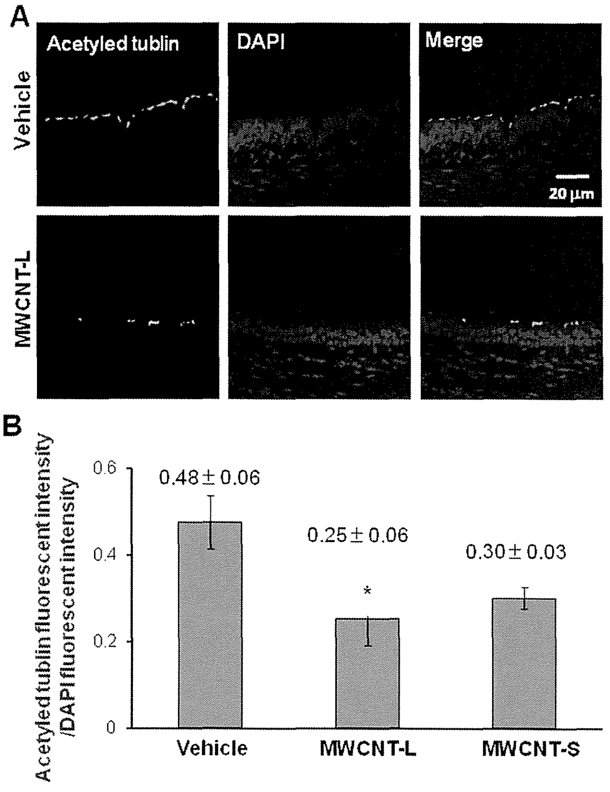

Fig. 5. Decrease in the proportion of ciliated cells in the bronchial epithelium. A, Representative images of immunostaining with anti-acetylated tubulin staining the cilia (left), DAPI (middle) and merged image (right); B, The ratio of the intensity of acetyled tublin to DAPI was decreased in the MWCNT-L group. n = 3~4; * $p < 0.05$ vs the vehicle.

DISCUSSION

The tracheobronchial ciliated epithelium is the first defense line against inhaled dust particles. The dust particles are transported from the lung alveoli through the bronchi and trachea toward the laryngopharynx by its directed ciliary movement. Pathologic changes in the bronchial epithelium such as goblet cell hyperplasia and squamous cell metaplasia have been found by studies

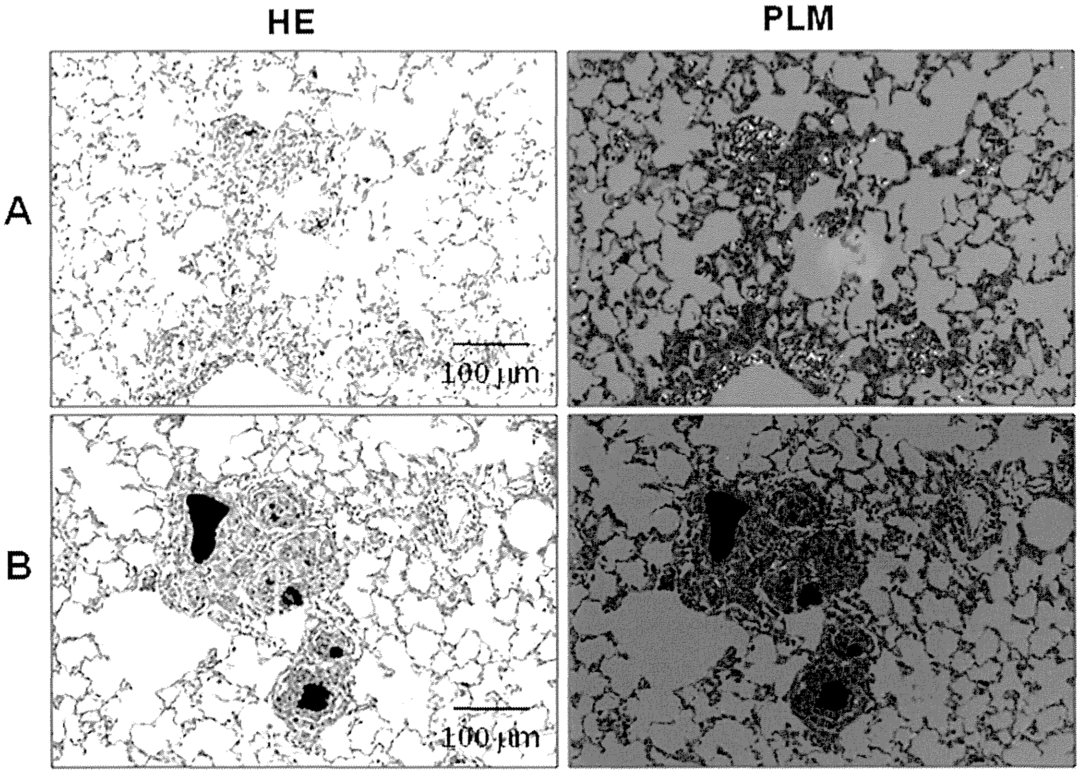

Fig. 6. Demonstration of MWCNTs in the lung tissue. HE and polarized images of the lung tissue treated with MWCNT-L (A) or MWCNT-S (B). Large aggregations of MWNNT-S (black mass) are found encapsulated in granulation tissue and small particles are found in alveolar macrophages. As in the trachea, MWCNT-S is not visualized by polarized light microscopy (PLM).

with particles such as ZnO particles (Choe *et al.*, 1997) and cigarette smoke (Neugut, 1988) and in some disease conditions such as bronchial asthma and chronic bronchitis (Aikawa *et al.*, 1992). The ciliated cell damage in these lesions causes impaired mucociliary protection and increases deposition of particles and microorganisms in the lung, causing inflammatory changes. These alterations may cause chronic injury and cell regeneration leading to an increase in carcinogenesis in the trachea, bronchi and lung.

This is the first report to show that MWCNTs cause extensive damage and loss of ciliated epithelium in the trachea followed by compensatory regeneration of cells without cilia including metaplastic squamous cells. *In vitro* observation clearly indicated that MWCNT caused impaired function of ciliated cells, potentially resulting in decreased clearance of the fibers from the lung, such as observed in studies of other fibers such as asbestos (Woodworth *et al.*, 1983). Decreased clearance of MWCNT would increase the retention time of the MWCNTs in the trachea and lung, which, in turn, would maintain the toxic effect, leading to even more loss of ciliated cells. This would increase the risk of spread of MWCNT to other organs, especially to the pleural cavity.

It should be noted that damage to the lung differed in MWCNT-L and MWCNT-S administered rats. Inflammatory changes, as evinced by an increase in granulation tissue in the lung, were more extensive in MWCNT-S administered rats. This indicates that there is an organotropic toxic effect of MWCNT. This may be related to their size and shape; however, further studies are necessary to elucidate the mechanism of this difference.

AKNOWLEDGMENTS

This study was supported by Grants-in-Aids by the Ministry of Health, Labour and Welfare, Japan: Risk of Chemical Substance 21340601 (H22-kagaku-ippan-005) and 2524301 (H25-kagaku-ippan-004).

REFERENCES

Aikawa, T., Shimura, S., Sasaki, H., Ebina, M. and Takishima, T. (1992): Marked goblet cell hyperplasia with mucus accumulation in the airways of patients who died of severe acute asthma attack. Chest, **101**, 916-921.

Bonner, J.C. (2010): Nanoparticles as a potential cause of pleural and interstitial lung disease. Proc. Am. Thorac. Soc., **7**, 138-141.

Cho, W.S., Duffin, R., Howie, S.E., Scotton, C.J., Wallace, W.A., Macnee, W., Bradley, M., Megson, I.L. and Donaldson, K. (2011): Progressive severe lung injury by zinc oxide nanoparticles; the role of Zn2+ dissolution inside lysosomes. Part Fibre. Toxicol., **8**, 27.

Choe, N., Tanaka, S., Xia, W., Hemenway, D.R., Roggli, V.L. and Kagan, E. (1997): Pleural macrophage recruitment and activation in asbestos-induced pleural injury. Environ. Health Perspect., **105 Suppl. 5**, 1257-1260.

Donaldson, K., Murphy, F.A., Duffin, R. and Poland, C.A. (2010): Asbestos, carbon nanotubes and the pleural mesothelium: a review of the hypothesis regarding the role of long fibre retention in the parietal pleura, inflammation and mesothelioma. Part. Fibre. Toxicol., **7**, 5.

Hirano, S., Fujitani, Y., Furuyama, A. and Kanno, S. (2010): Uptake and cytotoxic effects of multi-walled carbon nanotubes in human bronchial epithelial cells. Toxicol. Appl. Pharmacol., **249**, 8-15.

Li, J., Kanju, P., Patterson, M., Chew, W.L., Cho, S.H., Gilmour, I., Oliver, T., Yasuda, R., Ghio, A., Simon, S.A. and Liedtke, W. (2011): TRPV4-mediated calcium influx into human bronchial epithelia upon exposure to diesel exhaust particles. Environ. Health Perspect., **119**, 784-793.

Lindberg, H.K., Falck, G.C., Suhonen, S., Vippola, M., Vanhala, E., Catalan, J., Savolainen, K. and Norppa, H. (2009): Genotoxicity of nanomaterials: DNA damage and micronuclei induced by carbon nanotubes and graphite nanofibres in human bronchial epithelial cells *in vitro*. Toxicol. Lett., **186**, 166-173.

Ma, W., Korngreen, A., Weil, S., Cohen, E.B., Priel, A., Kuzin, L., and Silberberg, S.D. (2006): Pore properties and pharmacological features of the P2X receptor channel in airway ciliated cells. J. Physiol., **571**, 503-517.

Mercer, R.R., Hubbs, A.F., Scabilloni, J.F., Wang, L., Battelli, L.A., Schwegler-Berry, D., Castranova, V. and Porter, D.W. (2010): Distribution and persistence of pleural penetrations by multi-walled carbon nanotubes. Part. Fibre. Toxicol., **7**, 28.

Mercer, R.R., Scabilloni, J.F., Hubbs, A.F., Wang, L., Battelli, L.A., McKinney, W., Castranova, V. and Porter, D.W. (2013): Extrapulmonary transport of MWCNT following inhalation exposure. Part. Fibre. Toxicol., **10**, 38.

Nagai, H. and Toyokuni, S. (2010): Biopersistent fiber-induced inflammation and carcinogenesis: lessons learned from asbestos toward safety of fibrous nanomaterials. Arch. Biochem. Biophys., **502**, 1-7.

Neugut, A.I. (1988): Squamous cell cancers and cigarette smoke: a matter of exposure. Med. Hypotheses., **26**, 9-10.

Rotoli, B.M., Bussolati, O., Bianchi, M.G., Barilli, A., Balasubramanian, C., Bellucci, S. and Bergamaschi, E. (2008). Non-functionalized multi-walled carbon nanotubes alter the paracellular permeability of human airway epithelial cells. Toxicol. Lett., **178**, 95-102.

Simet, S.M., Sisson, J.H., Pavlik, J.A., Devasure, J.M., Boyer, C., Liu, X., Kawasaki, S., Sharp, J.G., Rennard, S.I. and Wyatt, T.A. (2010): Long-term cigarette smoke exposure in a mouse model of ciliated epithelial cell function. Am. J. Respir. Cell. Mol. Biol., **43**, 635-640.

Woodworth, C.D., Mossman, B.T. and Craighead, J.E. (1983): Squamous metaplasia of the respiratory tract. Possible pathogenic role in asbestos-associated bronchogenic carcinoma. Laboratory investigation; a journal of technical methods and pathology, **48**, 578-584.

Xu, J., Futakuchi, M., Alexander, D.B., Fukamachi, K., Numano, T., Suzui, M., Shimizu, H., Omori, T., Kanno, J., Hirose, A. and Tsuda, H. (2014): Nanosized zinc oxide particles do not promote DHPN-induced lung carcinogenesis but cause reversible epithelial hyperplasia of terminal bronchioles. Arch. Toxicol., **88**, 65-75.

Xu, J., Futakuchi, M., Shimizu, H., Alexander, D.B., Yanagihara, K., Fukamachi, K., Suzui, M., Kanno, J., Hirose, A., Ogata, A., Sakamoto, Y., Nakae, D., Omori, T. and Tsuda, H. (2012): Multi-walled carbon nanotubes translocate into the pleural cavity and induce visceral mesothelial proliferation in rats. Cancer Sci., **103**, 2045-2050.

ONCOLOGY LETTERS 9: 2112-2118, 2015

In vivo ^{18}F-fluorodeoxyglucose-positron emission tomography/computed tomography imaging of pancreatic tumors in a transgenic rat model carrying the human $KRAS^{G12V}$ oncogene

KOJI SHIBATA[1,2], KATSUMI FUKAMACHI[1], ATSUSHI TSUJI[3], TSUNEO SAGA[3],
MITSURU FUTAKUCHI[1], MASATO NAGINO[2], HIROYUKI TSUDA[4] and MASUMI SUZUI[1]

[1]Department of Molecular Toxicology, Nagoya City University Graduate School of Medical Sciences and Medical School,
Nagoya, Aichi 467-8601; [2]Division of Surgical Oncology, Department of Surgery,
Nagoya University Graduate School of Medicine, Nagoya, Aichi 466-8550; [3]Diagnostic Imaging Program,
Molecular Imaging Center, National Institute of Radiological Sciences, Chiba, Chiba 263-8555;
[4]Laboratory of Nanotoxicology Project, Nagoya University, Nagoya, Aichi 467-8603, Japan

Received March 25, 2014; Accepted December 19, 2014

DOI: 10.3892/ol.2015.3053

Abstract. A novel *KRAS*-mediated transgenic rat model has previously been demonstrated, in which animals develop multiple pancreatic ductal adenocarcinoma (PDAC) that is histologically similar to human PDAC within two weeks. Positron emission tomography (PET)/computed tomography (CT) is commonly used for the diagnosis and staging of PDAC in humans, and can be adopted for optimal use in animal experiments. The aim of the present study was to evaluate the carcinogenic process in a rat pancreatic carcinoma model using small-animal multimodality imaging systems. The utility of fluorodeoxyglucose (FDG)-PET/CT in detecting the location and size of PDAC during tumor development in the present transgenic rat model was assessed. A small animal multimodality PET/CT system and contrast-enhanced CT (CECT) system were used for the imaging analysis of $KRAS^{G12V}$ male transgenic rats (n=6), which developed pancreatic tumors following the administration of an injection of Cre recombinase (Cre)-carrying adenovirus. Laparotomies performed at six weeks post-treatment revealed that all three (100%) Cre-expressing rats developed pancreatic tumors that were <2 mm in diameter, none of which were detected by ^{18}F-FDG PET/CT or CECT. At eight weeks post-treatment, the pancreatic tumors were heterogeneously visualized by ^{18}F-FDG-PET/CT and CECT in two of the three rats. Furthermore, the autopsies confirmed that all three rats had developed pancreatic tumors. These novel findings provide evidence that the FDG-PET/CT imaging system is a valuable tool for the evaluation of the carcinogenic process, and one which may aid in treatment and preventive methods for pancreatic tumors in mammalian models. A limitation associated with the early detection of PDACs warrants further investigation.

Introduction

With >250,000 annual mortalities, pancreatic carcinoma is one of the most lethal malignancies, ranking 12th worldwide (1). Mortality resulting from this disease is high even in developed countries, including Japan, the United Kingdom, France and the United States (2,3). Overall, >75% of pancreatic carcinoma cases are histologically characterized as pancreatic ductal adenocarcinoma (PDAC) (4,5). The majority of cases of PDAC are incurable due to the necessity of extensive resection, which is often not feasible, and due to the fact that the disease is rarely identified at an early stage. Furthermore, the majority of patients with advanced PDAC either do not respond, or respond transiently to chemotherapeutic drugs and radiation (6). Typically, the majority of patients with PDAC succumb to the disease within one year of diagnosis, and the overall five-year survival rate is <5% (7). Even in patients with resectable carcinoma, the long-term outcome remains unsatisfactory due to the incidence of early recurrence following surgical resection.

In order to gain an improved understanding of this lethal malignant carcinoma, studies that use animal PDAC models with pancreatic neoplasms that resemble human PDAC are usually desirable. By focusing on human pancreatic adenocarcinomas that express a high frequency of *KRAS* mutation, a transgenic rat model carrying the human $HRAS^{G12V}$ or $KRAS^{G12V}$ oncogene was established (8,9). The activation of the target transgene is attained by the injection of a Cre recombinase (Cre)-carrying adenovirus into the pancreatic ducts of the animal via the

---

Correspondence to: Dr Masumi Suzui, Department of Molecular Toxicology, Nagoya City University Graduate School of Medical Sciences and Medical School, 1 Kawasumi, Mizuho-cho, Mizuho-ku, Nagoya, Aichi 467-8601, Japan
E-mail: suzui@med.nagoya-cu.ac.jp

Key words: carcinogenesis, positron emission tomography/computed tomography, ^{18}F-fluorodeoxyglucose, laparotomy, pancreatic tumor, rat model

common bile duct (8,9). In this model, the transgenic rats usually develop pre-neoplastic and neoplastic pancreatic lesions within two weeks of the viral inoculation (10). These lesions in the transgenic rats exhibit morphological similarities to those observed in human pancreatic lesions, including PDAC (11) and intraepithelial neoplasias (PanINs) (9).

Due to the position of the tumors within the abdominal cavity, laparotomy is the only technique that is able to determine the existence and size of pancreatic tumors within the transgenic rats following virus inoculation, as the tumors cannot be visually assessed from surface scans of the affected rats. A previous study determined that in order to serologically detect early-stage PDAC in the rat models, serum N-ERC levels and the levels of several serum miRNAs, which are expressed differentially in PDAC transgenic rats and control rats, could be used (8,12). However, even in the case of elevated levels of high serum biomarkers, the exact location and size of pancreatic tumors is difficult to detect unless exploratory surgery is performed within the abdominal cavity.

^{18}F-fluorodeoxyglucose-positron emission tomography ([^{18}F-FDG-PET) is commonly used during the diagnosis of pancreatic tumors (13,14). Due to a high sensitivity and penetration depth, PET is considered to be more accurate for the detection and identification of metastases in humans and animal models than other imaging systems (15,16).

The objective of the present study was to evaluate the carcinogenic process in a mammalian model using imaging modalities, such as PET/computed tomography (CT), which are applicable for the study of human PDAC.

Materials and methods

Animals. In total, six male *KRAS*^{G12V} oncogene transgenic rats were used in the present study. Routine genotyping was performed as previously described (8). The rats were kept in plastic cages in an air-conditioned room at 24±2°C and 60±5% humidity with a 12-h light/12-hour dark cycle. A basal diet (Oriental Yeast Co., Ltd., Tokyo, Japan) and tap water were available *ad libitum* throughout the experiment. All experiments were approved by the Animal Care and Use Committee of Nagoya City University Graduate School of Medical Sciences and the National Institute of Radiological Sciences (Tokyo, Japan).

Procedure of adenovirus inoculation. The preparation and inoculation of the adenoviruses was performed as previously described (9). In brief, a Cre-recombinase expressing adenovirus was amplified in HEK293 cells and then purified using the Vivapure AdenoPACK (Vivascience, Hannover, Germany) (17). The titer of the adenovirus was then determined using an Adeno-X rapid titer kit (Clontech, Mountain View, CA, USA). The virus was prepared to a concentration of $4.0\text{x}10^9$ plaque-forming units/ml. The virus (300-400 μl) was injected using a small syringe into the pancreatic duct of the rats as previously described (9).

[^{18}F-FDG-PET and CT procedures, and image analysis. The time course of the experimental protocol is shown in Fig. 1. For the present study, 10-week-old male *KRAS*^{G12V} transgenic rats were used. The rats were divided into two groups, with three rats per group. The rats in groups 1 and 2 were administered with the Cre-expressing adenovirus vector or an empty vector (negative control), respectively. A small-animal multimodality PET system (Inveon; Siemens Healthcare Inc., Malvern, PA, USA) was used for PET data acquisition. Following an overnight fast, each rat (body weight, 403-583 g) was injected with 15 MBq (14.6±1.6 MBq) ^{18}F-FDG (Nihon Medi-Physics Co., Ltd., Tokyo, Japan) via the tail vein, whilst the rat was under isoflurane anesthesia. The PET data acquisition was conducted for 10 min, beginning 50 min after the ^{18}F-FDG injection. Using a lamp, the body temperature of the rats was maintained at between 36 and 37°C during the scan. The images were reconstructed using a 3D maximum *a posteriori* (18 iterations with 16 subsets; β=0.2), without attenuation correction. The tracer uptake was expressed as the standardized uptake value (SUV).

Subsequent to PET scanning, plain or contrast-enhanced CT (CECT) was conducted with an X-ray source set at 90 kVp and 200 μA, using a small-animal CT system (R_mCT2; Rigaku, Tokyo, Japan). For CECT, the rats were intravenously injected with 10 ml Iopamiron 370 contrast medium (Bayer Yakuhin Ltd., Osaka, Japan) using an infusion pump (NE-1000; Neuroscience Inc., Tokyo, Japan) at the rate of 2 ml/min, whilst the rats were under isoflurane anesthesia. The CECT images were acquired 5 min subsequent to the injection. In order to reduce the motion artifacts caused by respiratory and peristaltic movement during the CT scan, a respiratory gating system was used whilst the rats under inhalable isoflurane anesthesia. The ^{18}F-FDG-PET scanning was conducted at two, three, four, five and eight weeks subsequent to administration of the Cre-expressing adenovirus or the empty vectors. In order to confirm the results of the PET analysis, the CECT scan was also conducted at five and eight weeks subsequent to the virus injection. For the quantitative analysis, the PET and CT data sets were imported and the fused images were then obtained using ASIPro VM software (CTI Concorde Microsystems, Knoxville, TN, USA). Laparotomy was performed six weeks subsequent to the injection in order to confirm the location and size of the pancreatic tumors, which were visible to the naked eye. The experimental rats were sacrificed eight weeks subsequent to the injection.

Histopathological examination. The rats in groups 1 and 2 survived until the end of the experimental period. The pancreatic tumors and the normal pancreatic lobes were removed from the abdomen of the rats, fixed with 10% buffered formalin and then processed for histopathological examination using hematoxylin and eosin stain (9). The pancreatic lesions were diagnosed histopathologically based upon previously described criteria (8,9).

Results

PET/CT findings and histopathological examination. The six rats were euthanized eight weeks subsequent to the injection of the Cre-expressing viral or empty vectors. All three Cre-expressing transgenic rats in group 1 (100%) developed orthotopic pancreatic tumors without distant metastasis. By contrast, no tumors were identified in the negative control rats of group 2. Upon macroscopic analysis, the tumors appeared nodular and solid in shape, and were ochre yellow in color. The

Table I. Mean SUV of the tumor and each organ in the experimental rats.

Rat	Tumor (SUV_{max})	GI tract (SUV_{max})	Liver	Kidney (cortex and medulla)
1	0.7-1.2 (1.4)	0.5-1.0 (3.2)	0.4-0.5	0.8-0.9
2	0.9-2.0 (3.0)	0.5-1.8 (2.7)	0.5-0.6	0.9-1.1
3	ND	0.6-1.4 (4.2)	0.6-0.7	0.9-1.1

The rats were inoculated with a Cre recombinase-expressing vector as described in the Materials and methods section. The values were calculated using the scanning data obtained at eight weeks post-inoculation. SUV_{max}, maximum standardized uptake value; GI, gastrointestinal; ND, Not detected.

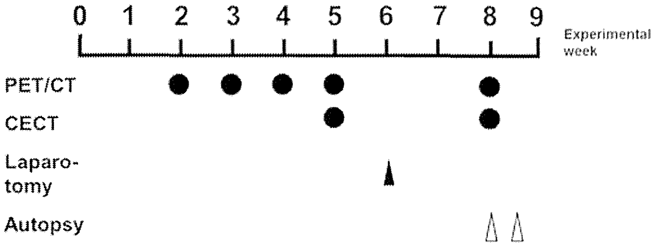

Figure 1. Experimental time course. Closed circle indicates the time of scanning. Closed triangle indicates the time of laparotomy. Open triangle indicates the time of autopsy. Laparotomy and autopsy were performed on the three rats from group 1 at eight weeks post-viral inoculation. Viral inoculation was performed at week zero. PET, positron emission tomography; CT, computed tomography; CECT, contrast-enhanced computed tomgraphy.

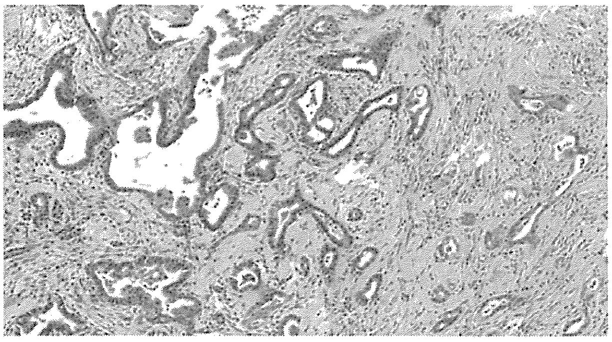

Figure 2. Representative microscopic image of a pancreatic ductal adenocarcinoma, revealing papillotubular growth of the tumor cells and abundant fibrous tissue proliferation (hematoxylin and eosin staining; magnification, x100).

PET/CT images obtained eight weeks subsequent to the viral injection revealed the majority of tumor tissues to be distinguishable from the adjacent organs, but the tissues were challenging to distinguish from the normal intestinal tissues, depending on the site of the tumor. The pancreatic tumors were of the ductal adenocarcinoma histological type. The coexistence of adenocarcinoma and PanIN lesions surrounded by fibrous tissue with inflammatory cell infiltration was also identified (Fig. 2).

[^{18}F-FDG-PET imaging prior to experimental week five. The representative maximal-intensity projection images from ^{18}F-FDG-PET are shown in Fig. 3. PET scanning was performed four times prior to the five experimental weeks. A marginal or very high uptake in the gastrointestinal tract and urinary bladder, which was considered to be physiological FDG uptake, was observed in all three Cre-expressing transgenic rats and three control rats. At five weeks post-treatment, the tumors were not clearly visualized by the indicated imaging system. Following the laparotomy at six weeks post-treatment, a few small nodules measuring between 1 and 2 mm in diameter, indicative of a carcinoma, were identified in the pancreas of all Cre-expressing transgenic rats. No metastases were identified in the rats of the negative control group.

Analysis of CECT, PET and PET/CT images at eight weeks post-treatment. Representative slices of the ^{18}F-FDG-PET/CT fusion images obtained from the Cre-expressing transgenic rats are shown in Figs. 4-6. The SUV_{max} and SUV_{mean} of the pancreatic tumors and each organ are shown in Table I. In rat 1 (body weight, 503 g), the CECT images revealed a heterogeneous lesion measuring 17 mm in the maximum sagittal diameter in the left side of the abdomen. In addition, the PET and PET/CT fusion images revealed moderately increased ^{18}F-FDG uptake in the lesion located in the left side of the abdomen, with a SUV_{max} of <1.5. Physiological FDG uptake was observed in the gastrointestinal tract, and the SUV_{max} of this organ site was 3.2, as shown in Table I. Autopsy revealed a large tumor in the splenic lobe, which was detected by CECT and PET/CT. However, multiple tumors that were present in the duodenal lobe of the pancreas were not revealed by CECT and PET/CT (Fig. 4). In rat 2 (body weight, 470 g), the CECT images revealed a heterogeneously-enhanced pancreatic tumor, measuring 20 mm in the maximum sagittal diameter, in the left side of the abdomen. PET/CT fusion images revealed moderate uptake of ^{18}F-FDG (SUV_{max}, 3.0) in the pancreatic tumor. In addition, physiological FDG uptake in the gastrointestinal tract (SUV_{max}, 2.7) was observed. During autopsy, a large tumor in the splenic lobe was identified by the imaging analysis. In addition, multiple tumors were identified in the duodenal lobe of the pancreas, but these tumors were not visualized on CECT and PET/CT (Fig. 5). In rat 3 (body weight, 564 g), the presence of a tumor was not observed on either CECT or PET scans (Fig. 6). Next, an incision was made in the abdomen of the rat, and a number of nodules, which were smaller in size than those observed in rats no. 1 and 2, were identified in the

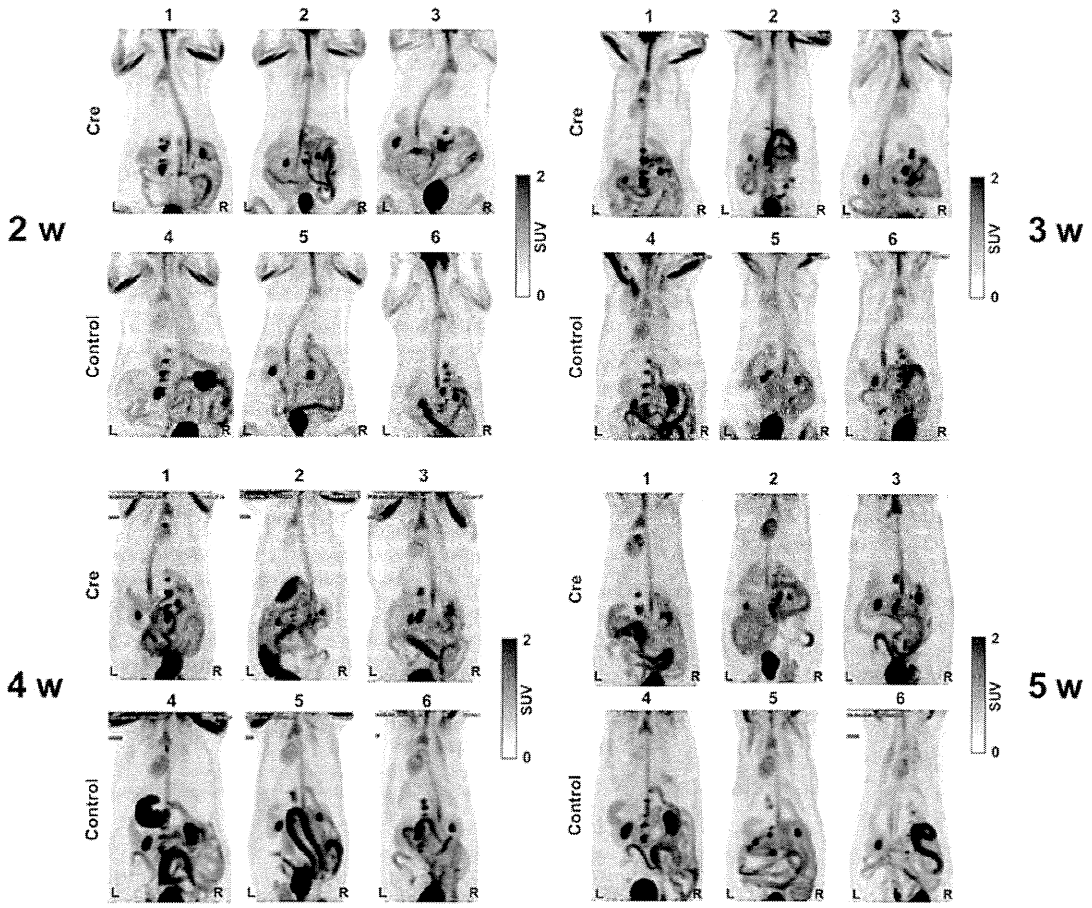

Figure 3. Representative positron emission tomography (PET) images of the transgenic rats at a maximum intensity projection. Images were obtained from Cre recombinase (Cre)-expressing transgenic rats (1-3) and control rats (4-6). Scanning was performed at two, three, four and five weeks post-viral inoculation. Subsequent to fasting, the rats were injected under isoflurane anesthesia with ~15 MBq ^{18}F-fluorodeoxyglucose (FDG) via the tail vein. PET data was acquired 50 min post-injection. Physiological FDG uptake was observed in the intestines, kidney and urinary bladder, but no tumor masses were identified in any of the images. L, left side; R, right side. SUV, standardized uptake value; w, weeks.

duodenal lobe of the pancreas. No tumor was identified in the splenic lobe of the pancreas. No macroscopic metastasis was identified in rats 1-3.

Discussion

A limited number of the documented studies that involve imaging analysis of pancreatic tumors in animal models used the FDG-PET/CT system (18,19). In the present study, a *KRAS*-mediated transgenic rat model was used to develop multiple pancreatic tumors that resembled the developmental and histological features of human PDAC within two weeks (8). In living rats at eight weeks post-treatment, the pancreatic tumors were clearly enhanced in the CECT images following the administration of a contrast media, and were distinguishable from the gastrointestinal tract. In the absence of imaging analysis, calipers are used to determine the location and size of a pancreatic tumor following a laparotomy or autopsy of an animal. Imaging analysis therefore allows each animal to be scanned sequentially in a sectional plane of interest, such as transverse, coronal or sagittal, and be monitored over time without the need to be sacrificed. In addition, PET/CT enables the accurate measurement of irregularly-shaped tumors in a pancreatic tumor model. According to the Three Rs principle (20), which aims to replace existing experimental methods with those that do not use animals, reduce the number of test animals used and refine methods in order to minimize the suffering of test animals, the PET/CT system reduces the number of animals required for experimental treatment and control groups. This indicates that imaging systems should be recommended for use in animal experiments. Recently, inoculation efficacy has been improved by clamping the common bile duct and increasing the amount of virus that is administered. Using this technique, studies may be able to control the size of the pancreatic tumor quantitatively within an appropriate time period, a factor that demonstrates the usefulness of this model.

With regard to studies that have used small animal models, Kitahashi *et al* (21) used micro-CT to detect chemically-induced pancreatic tumors of >4 mm in diameter in Syrian hamsters. Another study by Fendrich *et al* (18) detected precursor pancreatic adenocarcinoma lesions with an activity of 9.6±0.5 MBq in a five-month-old transgenic mouse model by FDG-PET/CT. Kayed *et al* (22) measured the anticancer effects of cyclopamine in a pancreatic carcinoma xenograft with an activity of 7.4 MBq model using ^{18}F-PET/CT. The study examined the size and SUV of each

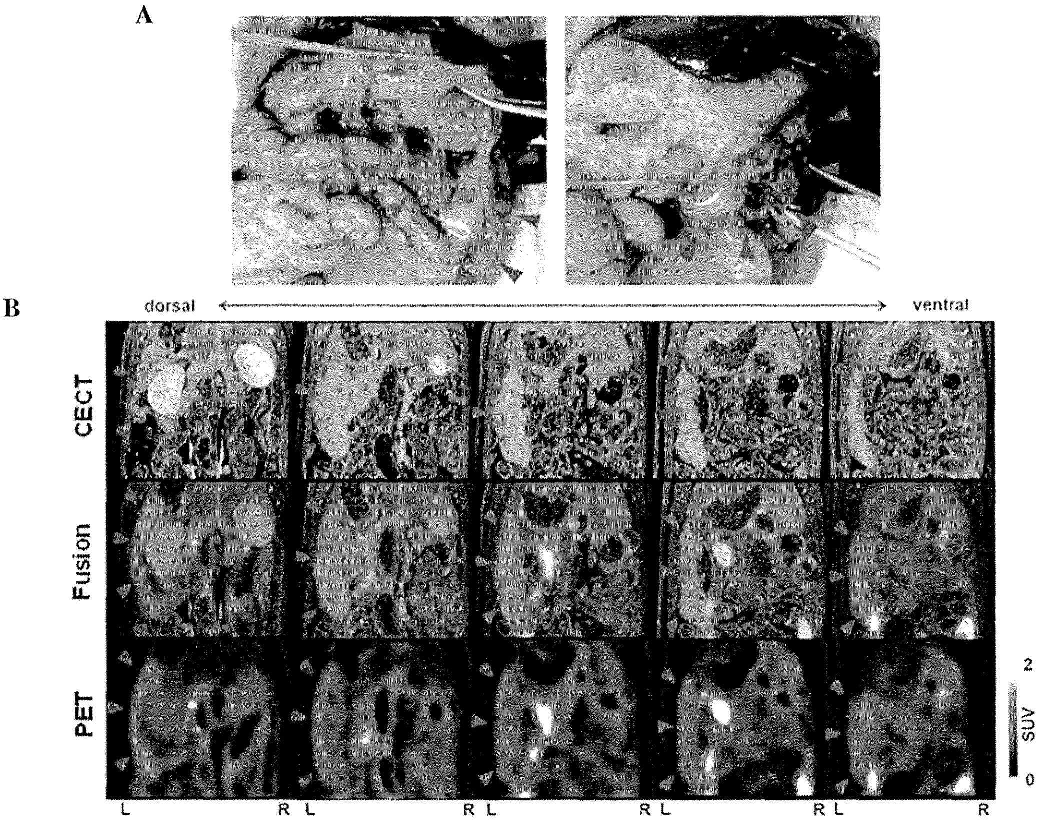

Figure 4. Autopsy view, positron emission tomography (PET)/contrast-enhanced CT (CECT) and PET/CECT fusion images of rat 1. (A) Tumors were observed in the duodenal lobe (left panel, red arrowheads) and the in splenic lobe (left and right panel, blue arrowheads) of the pancreas. (B) PET, CECT and PET/CECT fusion images revealed a large mass on the left side of the body (arrowheads). Physiological fluorodeoxyglucose uptake was also observed in the kidneys and intestines. L, left side; R, right side; SUV, standardized uptake value.

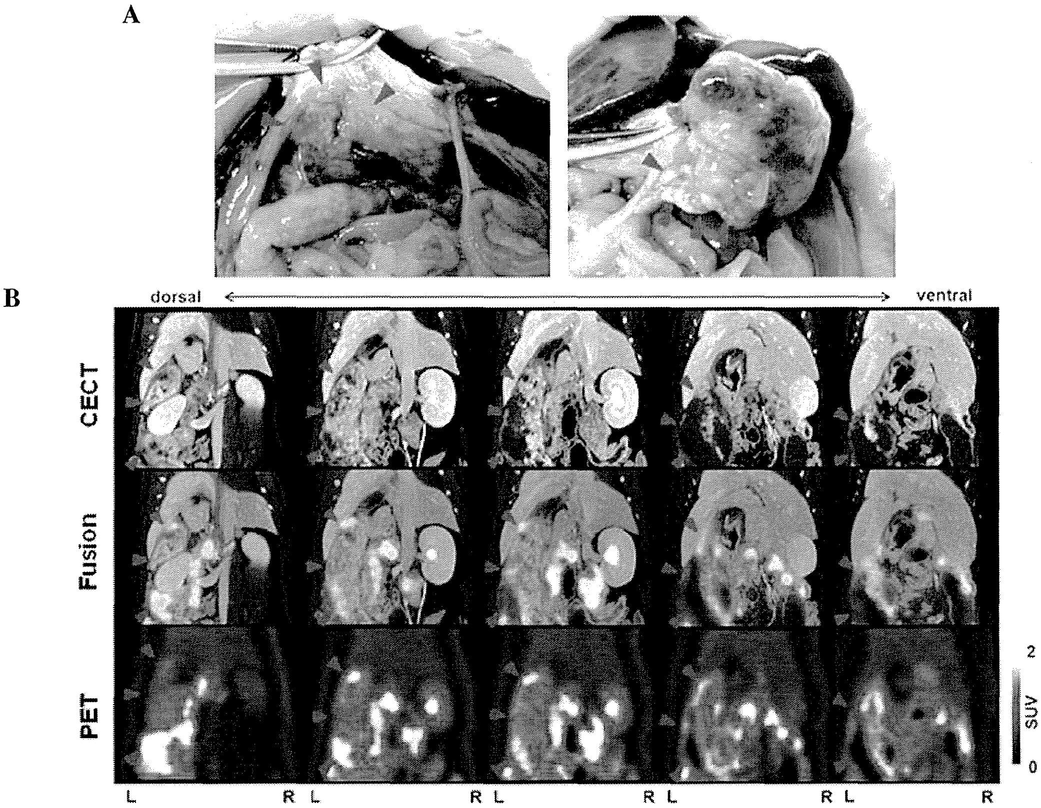

Figure 5. Autopsy view, positron emission tomography (PET), contrast-enhanced CT (CECT) and PET/CECT fusion images of rat 2. (A) Tumors were observed in the duodenal lobe (left and right panels, arrowheads) of the pancreas. The liver was intact. (B) PET, CECT and PET/CECT fusion images revealed multiple tumor masses in the left side of the body (arrowheads). L, left side; R, right side; SUV, standardized uptake value.

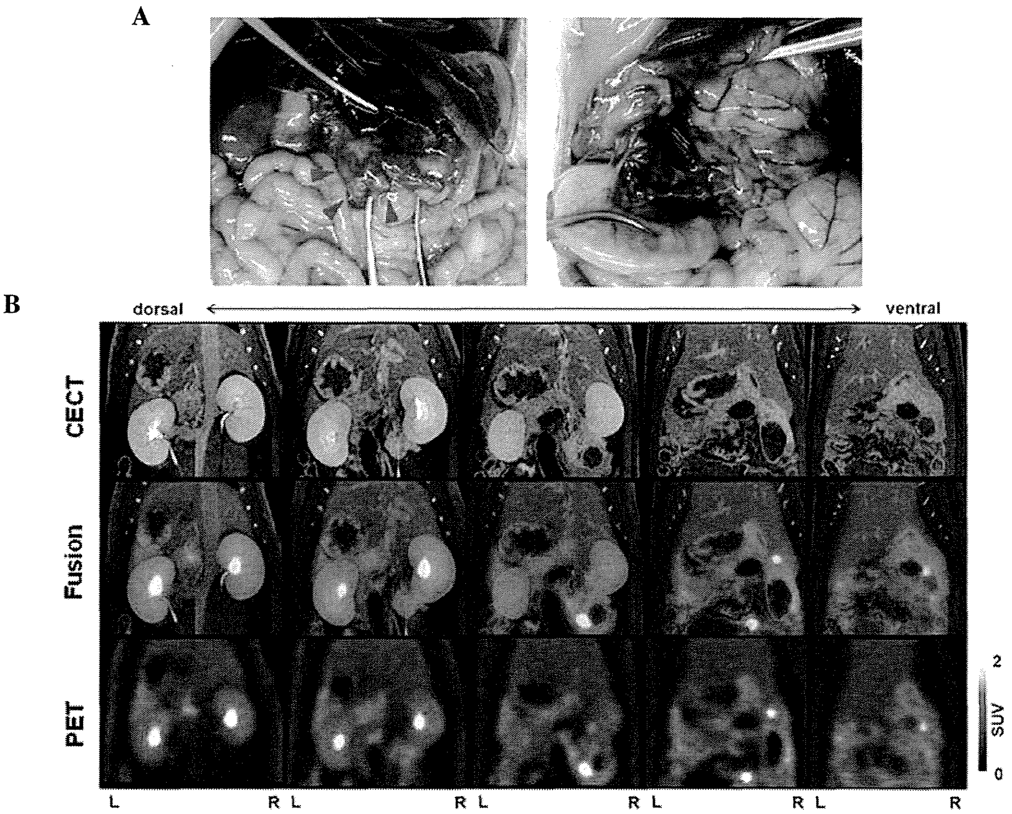

Figure 6. Autopsy view, positron emission tomgraphy (PET), contrast-enhanced CT (CECT) and PET/CECT fusion images of rat 3. (A) Tumors were observed in the duodenal lobe (left panel, arrowheads), but not in the splenic lobe of the pancreas. (B) No tumor-like lesions were revealed in the PET/CT and CECT images. SUV, standardized uptake value; R, right side; L, left side.

tumor that was grown in the hip region of nude mice during a seven-day treatment period. A technical limitation in baseline calibration occurred, but the system was believed to be suitable for practical use. The SUV and SUV_{max} parameters have been demonstrated in a previous study to be potential predictors of early recurrence following the curative resection of lung carcinomas (23).

It was hypothesized that the amount of FDG uptake into the pancreatic tumors would be higher compared with other abdominal organs. However, the results shown in Table I indicate that each value was not necessarily specific to the region of interest. This indicates a limitation in the use of this parameter for differential diagnoses that are based upon imaging techniques. To avoid bias during the measurement of the SUV, representative areas of tumor tissues that demonstrated moderate FDG uptake were selected. Therefore, the potential limitations of this methodology should be considered when calculating the SUV or SUV_{max}. This aspect warrants further investigation.

PET images did not identify tumor masses in any organ of the Cre-expressing rats until five weeks post-treatment (Fig. 3). When the laparotomy was performed six weeks subsequent to the viral inoculation, multiple tumors measuring <2 mm in diameter were identified in the pancreas of all three Cre-expressing transgenic rats. This indicated that the transgenic rats developed macroscopically visible tumors by six weeks post-treatment. At eight weeks post-treatment, the PET/CT images revealed pancreatic tumor masses in two of the three rats, which indicated a potential limitation in the detection of tumors prior to the eighth week by current imaging techniques. Pancreatic tumors were primarily identified in the splenic lobe of the pancreas by PET/CT. Tumors in the duodenal lobe, however, could not be detected by such imaging analyses, even if these tumors were confirmed by laparotomy. In addition, the presence of smaller tumors, and a specific anatomical location within the gastrointestinal tract, may affect the visibility of the tumor. In the PET and PET/CT fusion images, the pancreatic tumors were visible, but the physiological ^{18}F-FDG uptake in the intestine reduced the appearance of the lesions.

In conclusion, the present study demonstrated that pancreatic tumors can be detected in rats using imaging modalities eight weeks after viral inoculation. The FDG-PET/CT imaging system is a valuable approach for the evaluation of the carcinogenic process and potential treatment or prevention methods for pancreatic tumors in mammalian models. Therefore, it is proposed that this experimental system can also be applied to studies that examine cases of human PDAC.

Acknowledgements

The authors would like to thank Maki Okada for providing technical assistance with the CECT scanning, Hidekatsu Wakizaka for providing operational and quality control support for the PET system and Nobuyuki Miyahara for providing quality control support for the CT system.

References

1. Ferlay J, Shin HR, Bray F, Forman D, Mathers C and Parkin DM: Estimates of worldwide burden of cancer in: GLOBOCAN 2008. Int J Cancer 127: 2893-2917, 2010.
2. Matsuda A, Matsuda T, Shibata A, Katanoda K, Sobue T and Nishimoto H; Japan Cancer Surveillance Research Group: Cancer incidence and incidence rates in Japan in 2007: a study of 21 population-based cancer registries for the Monitoring of Cancer Incidence in Japan (MCIJ) project. Jpn J Clin Oncol 43: 328-336, 2013.
3. Bosetti C, Bertuccio P, Negri E, La Vecchia C, Zeegers MP and Boffetta P: Pancreatic cancer: overview of descriptive epidemiology. Mol Carcinog 51: 3-13, 2012.
4. Cubilla AL and Fitzgerald PJ: Cancer of the exocrine pancreas: the pathologic aspects. CA Cancer J Clin 35: 2-18, 1985.
5. Morohoshi T, Held G and Klöppel G: Exocrine pancreatic tumours and their histological classification. A study based on 167 autopsy and 97 surgical cases. Histopathology 7: 645-661, 1983.
6. Wolfgang CL, Herman JM, Laheru DA, *et al:* Recent progress in pancreatic cancer. CA Cancer J Clin 63: 318-348, 2013.
7. Siegel R, Naishadham D and Jemal A: Cancer statistics. CA Cancer J Clin 63: 11-30, 2013.
8. Fukamachi K, Tanaka H, Hagiwara Y, *et al:* An animal model of preclinical diagnosis of pancreatic ductal adenocarcinomas. Biochem Biophys Res Commun 390: 636-641, 2009.
9. Ueda S, Fukamachi K, Matsuoka Y, *et al:* Ductal origin of pancreatic adenocarcinomas induced by conditional activation of a human Ha-ras oncogene in rat pancreas. Carcinogenesis 27: 2497-2510, 2006.
10. Yabushita S, Fukamachi K, Tanaka H, *et al:* Metabolomic and transcriptomic profiling of human K-ras oncogene transgenic rats with pancreatic ductal adenocarcinomas. Carcinogenesis 34: 1251-1259, 2013.
11. Yabushita S, Fukamachi K, Kikuchi F, *et al:* Twenty-one proteins up-regulated in human H-ras oncogene transgenic rat pancreas cancers are up-regulated in human pancreas cancer. Pancreas 42: 1034-1039, 2013.
12. Yabushita S, Fukamachi K, Tanaka H, *et al:* Circulating microRNAs in serum of human K-ras oncogene transgenic rats with pancreatic ductal adenocarcinomas. Pancreas 41: 1013-1018, 2012.
13. Asagi A, Ohta K, Nasu J, *et al:* Utility of contrast-enhanced FDG-PET/CT in the clinical management of pancreatic cancer: impact on diagnosis, staging, evaluation of treatment response, and detection of recurrence. Pancreas 42: 11-19, 2013.
14. Tomimaru Y, Takeda Y, Tatsumi M, *et al:* Utility of 2-[18F] fluoro-2-deoxy-D-glucose positron emission tomography in differential diagnosis of benign and malignant intraductal papillary-mucinous neoplasm of the pancreas. Oncol Rep 24: 613-620, 2010.
15. Lan BY, Kwee SA and Wong LL: Positron emission tomography in hepatobiliary and pancreatic malignancies: a review. Am J Surg 204: 232-241, 2012.
16. Studwell AJ and Kotton DN: A shift from cell cultures to creatures: in vivo imaging of small animals in experimental regenerative medicine. Mol Ther 19: 1933-1941, 2011.
17. Kanegae Y, Lee G, Sato Y, *et al:* Efficient gene activation in mammalian cells by using recombinant adenovirus expressing site-specific Cre recombinase. Nucleic Acids Res 23: 3816-3821, 1995.
18. Fendrich V, Schneider R, Maitra A, Jacobsen ID, Opfermann T and Bartsch DK: Detection of precursor lesions of pancreatic adenocarcinoma in PET-CT in a genetically engineered mouse model of pancreatic cancer. Neoplasia 13: 180-186, 2011.
19. van Kouwen MC, Laverman P, van Krieken JH, Oyen WJ, Jansen JB and Drenth JP: FDG-PET in the detection of early pancreatic cancer in a BOP hamster model. Nucl Med Biol 32: 445-450, 2005.
20. Russell WMS and Burch RL (eds): The Principles of Humane Experimental Technique. 2nd edition. Methuen & Co, London, 1992.
21. Kitahashi T, Mutoh M, Tsurusaki M, *et al:* Imaging study of pancreatic ductal adenocarcinomas in Syrian hamsters using X-ray micro-computed tomography (CT). Cancer Sci 101: 1761-1766, 2010.
22. Kayed H, Meyer P, He Y, *et al:* Evaluation of the metabolic response to cyclopamine therapy in pancreatic cancer xenografts using a clinical PET-CT system. Transl Oncol 5: 335-343, 2012.
23. Sakai T, Tsushima T, Kimura D, Hatanaka R, Yamada Y and Fukuda I: A clinical study of the prognostic factors for postoperative early recurrence in patients who underwent complete resection for pulmonary adenocarcinoma. Ann Thorac Cardiovasc Surg 17: 539-543, 2011.

A Novel Transgenic Mouse Model Carrying Human Tribbles Related Protein 3 (TRB3) Gene and Its Site Specific Phenotype

Yuto Sakai,[a,b] Katsumi Fukamachi,[b] Mitsuru Futakuchi,[b] Ichiro Miyoshi,[c] Hiroyuki Tsuda,[d] Masumi Suzui,*[,b] and Hidetoshi Hayashi*[,a]

[a] *Department of Drug Metabolism and Disposition, Graduate School of Pharmaceutical Sciences, Nagoya City University;* [d] *Nanomaterial Toxicology Project, Nagoya City University; 3–1 Tanabe-dori, Mizuho-ku, Nagoya 467–8603, Japan:* [b] *Department of Molecular Toxicology, Graduate School of Medical Sciences and Medical School, Nagoya City University; and* [c] *Department of Comparative and Experimental Medicine, Graduate School of Medical Sciences and Medical School, Nagoya City University; 1 Kawasumi, Mizuho-cho, Mizuho-ku, Nagoya 467–8601, Japan.*

Received March 24, 2014; accepted March 31, 2014

Tribbles related protein 3 (TRB3) pseudokinase plays a crucial role in cell proliferation, migration and morphogenesis during development. In our recent study, an introduction of human TRB3 gene into mouse mammary tumor cells caused an increase of proliferation of tumor cells and their nuclear size. In the current study, to examine whether this gene causes *de novo* morphological changes in a specific organ site we have developed a novel variation of the transgenic mouse model that conditionally expresses human TRB3 (hTRB3) gene using Cre-recombinase (Cre)/loxP recombination system. By injecting hTRB3 transgene construct into pronuclei of mouse embryo, we eventually obtained four hTRB3 mice. The gene expression was controlled by infection of adenovirus-expressing Cre *via* the tail vein of hTRB3 mouse. In Cre-mediated hTRB3 mouse, expression of the hTRB3 protein was detected in the cytoplasm of hepatocytes in the liver. Expression of this protein was also seen in lymphocytes in the spleen, glomerular endothelial cells, and epithelial cells of collecting duct of the kidney. In hepatocytes of the hTRB3 mouse, nuclear size was significantly greater than that of the wild type mouse, indicating that hTRB3 can play a role at least in part in hepatic morphogenesis. The present animal model may provide a system for evaluation of *de novo* morphological changes induced by a specific transgene in a specific organ site.

Key words Tribbles related protein 3 (TRB3); transgenic mouse; Cre-recombinase (Cre)/loxP

Tribbles related protein 3 (TRB3) is one of the mammalian homologues of *Drosophila* Tribbles. This molecule contains a serine/threonine kinase catalytic domain but lacks an ATP binding site or one of the conserved catalytic motifs essential for kinase activity.[1–3)] TRB3 has also been shown to be involved in multiple cellular processes such as glucose/lipid metabolism, muscle/adipocyte differentiation, and stress response by interacting with various functional proteins.[1,3–10)] Three mammalian Tribbles homologues, TRB1, TRB2, and TRB3 are crucial modulators of tumorigenesis.[3,11–13)] TRB1 and TRB2 induce acute myelogenous leukemia by inhibiting CCAAT/enhancer binding protein α (C/EBPα) function.[12)] TRB3 is highly expressed in a wide range of human carcinoma cell lines and in several types of human carcinoma.[3,13)] We have recently demonstrated that TRB3 promotes proliferation and induces polyploidy of mouse mammary tumor cells.[14)] This finding was likely to indicate TRB3's response to morphological function. In the current study, by utilizing the recombinant adenovirus expressing Cre-recombinase (Cre) system we examined whether human TRB3 gene causes *de novo* morphological changes in a specific organ site.

MATERIALS AND METHODS

Generation of Human TRB3 Transgenic Mouse We ligated flag-tagged full length human TRB3 (hTRB3) cDNA[7)] into *Kpn*I and *Swa*I restriction sites of pCALNL5 vector (DNA Bank, RIKEN Bio Resource Center, Ibaraki, Japan),[15–17)] and this construct was termed pCALNL-flag-hTRB3. The pCALNL-flag-hTRB3 was digested at *Ssp*I/*Hin*dIII restriction sites.

African green monkey kidney fibroblast cell line COS7 was obtained from Cell Resource Center for Biomedical Research Institute of Development, Aging and Cancer, Tohoku University, Sendai, Japan and cultured in Dulbecco's modified Eagle's medium (DMEM) (Wako Pure Chemical Industries, Ltd., Osaka, Japan) containing 10% fetal bovine serum (FBS) (Life Technologies, Inc., Rockville, MD, U.S.A.). Expression vectors pCALNL-flag-hTRB3 (generated in this study), pcDNA3.1-flag-hTRB3 (used as positive control),[7)] pxCANCre (DNA Bank, RIKEN Bio Resource Center) and empty vector pCALNL5 (used as negative control) were transfected into COS7 cells using FuGENE6 reagent (Roche Diagnostics Corp., Indianapolis, IN, U.S.A.), and these cells were cultured in in a 6-cm culture dish. Using the transfected cells, levels of protein expression were confirmed by Western blot assays.

After confirming the Cre/loxP system functions by examining the expression status of hTRB3 that can be measured with Flag expression, the purified cassette (Fig. 1) was injected into the pronuclei of C57BL/6NCrSlc mouse (CLEA Japan, Tokyo, Japan). A total of 184 injected eggs were transplanted into pseudo-pregnant C57BL/6NCrSlc mouse. Of 8 potential transgenic mice screened, four mice were shown to carry the transgene by polymerase chain reaction (PCR) as described below. These four transgenic founder mice were then mated with wild type C57BL/6NCrSlc mice (wild mice) and offspring were screened for the presence of the transgene by PCR assay of genomic DNA isolated from tail

---

The authors declare no conflict of interest.

* To whom correspondence should be addressed. e-mail: suzui@med.nagoya-cu.ac.jp; hhayashi@phar.nagoya-cu.ac.jp

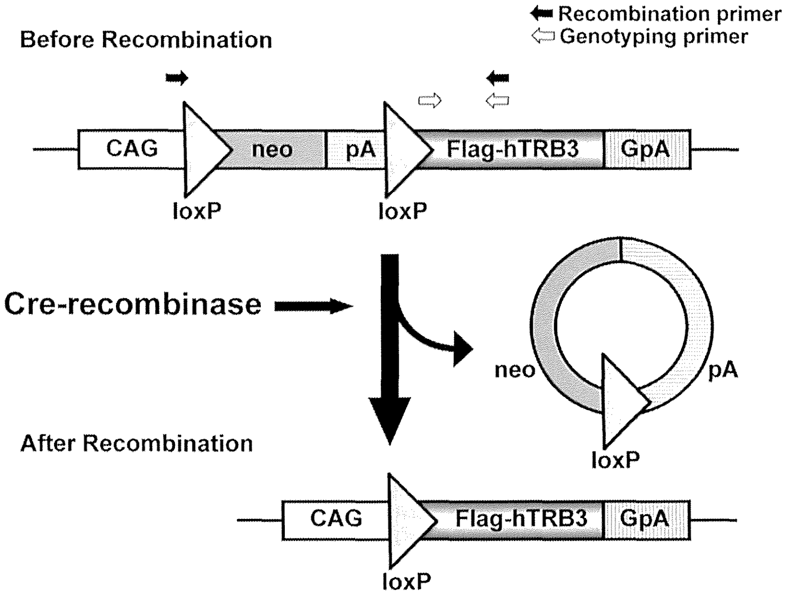

Fig. 1. Scheme of Recombination of hTRB3 Construct

The pCALNL-flag-hTRB3 construct is comprised of a hybrid CMV enhancer/chicken β-actin (CAG) promoter, a cassette for the neomycin resistance gene flanked by loxP sites, and a sequence containing a human TRB3 with a Flag-tag. Infection with the Cre expressing adenovirus results in recombination of hTRB3 construct, eventually generating a functional flag-hTRB3 gene expression unit. GpA, rabbit β-globin poly A site; pA, SV40 early poly A site.

biopsies at the age of 3 weeks. The following primers were used: geno-hTRB3F (5′-TGT CTG GAT CAA ATC CGA AC-3′) and geno-hTRB3R (5′-ATC CGT CGA CCC TTG TCA TC-3′). In the present study, we used these transgenic mice termed NCrSlcBL6-TgN(hTRB3) mice (hTRB3 mice). The mouse was maintained in plastic cages in an airconditioned room with a 12 h light/12 h dark cycle.

hTRB3 mouse embryonic fibroblast cell line (hTRB3 MEF) that carries human TRB3 gene was generated from hTRB3 mouse. MEF cell line was also generated from wild mouse. The hTRB3 female mouse was euthanized at 14 d postcoitum and embryos were removed from placenta. After excising head and viscera, the embryo was cut into small pieces until it became possible to pipette. One milliliter of trypsin/EDTA (Life Technologies) was added to one embryo and incubated at 37°C for 15 min. After adding DMEM containing 10% FBS, centrifugation was done and supernatant containing MEF cells was used for cell culture. MEF cell lines were cultured in DMEM containing 10% FBS.

To see whether the Cre/loxP system properly functions, we examined the expression status of mRNA and protein of hTRB3 in MEF cells. Adenovirus carrying the Cre gene (AxCANCre) was prepared as described previously.[15,16] Adenovirus vectors were amplified in HEK-293 cell line that was purchased from ATCC (Manassas, VA, U.S.A.), cultured in DMEM containing 10% FBS, and purified using Vivapure Adenopack (Vivascience, Hannover, Germany). The titer of the adenovirus was determined by using the Rapid titer kit (Clontech, Mountain View, CA, U.S.A.). The virus stock was concentrated to 1.0×10^{10} pfu per mL. MEF cells with or without hTRB3 transgene were infected with Cre expressing adenovirus (0, 100, 200 multiplicity of infection (MOI)) for 2 h. After the infection, cells were cultured in DMEM containing 10% FBS for 48 h, genomic DNA, total RNA, and protein were extracted and used for PCR, reverse transcription (RT)-PCR, and Western blot assays.

After confirming that the Cre/loxP system functions *in vitro*, the system was introduced into mice and initiated by infecting animals with Cre expressing adenovirus. Cre expressing adenovirus (1×10^{8} pfu/mouse) was injected into the tail vein of 4-week-old mouse. To induce Flag-tagged-human TRB3 gene, adenovirus in which the expression of Cre was under the control of the CAG promoter was used. Ten days after Cre expressing adenovirus was injected, all mice were euthanized and complete autopsy was done. Liver, spleen, and kidneys were carefully removed and processed for macroscopic examination and histopathological/immunohistochemical analyses. All experimental procedures conformed to the Regulations for Animal Experimentation at Nagoya City University were reviewed by the Institutional Laboratory Animal Care and Use Committee of Nagoya City University and finally approved by the President of University.

Immunohistochemical Analysis These assays were performed using an established method as described elsewhere.[18] Three-micrometer-thick paraffin sections were prepared from liver, spleen and kidney. These sections were treated in 3% H_2O_2 for 10 min to block the endogenous peroxidase activity. For antigen retrieval, the sections were brought to boiling in 0.1 M citrate buffer, pH 6.0. Sections were then incubated with a primary antibody (1 : 500 dilution) of the FLAG (Sigma, St. Louis, MO, U.S.A.) at room temperature for 1 h. After incubation with secondary antibody, sections were then stained using an ABC kit (Vector Laboratories Inc., Burlingame, CA, U.S.A.) according to the manufacturer's instructions. The number of Cre-treated wild mouse was one, and that of Cre-treated hTRB3 mice was eight. The number of untreated wild mouse was one and that of untreated hTRB3 mouse was also one. Each liver slide has two to four tissue slices. In the liver tissue slices of hTRB3 and wild mice, the longest diameter of nucleus of the liver cell was determined by image analysis (Olympus DP70 system, Olympus Corp., Tokyo, Japan). Four high power fields per liver tissue were examined and more than 100 nuclei were counted in each liver tissue.

RT-PCR and PCR Assays These assays were done with established procedures.[18] Total RNA was extracted from each cell line grown in 9-cm culture dishes using ISOGEN (Nippon Gene, Toyama, Japan). The reaction mixture contains 4 μg of total RNA, 1 μL of 10 mM deoxyribonucleotide triphosphate (dNTP) (Life Technologies), 1 μL of Random primers (Life Technologies) and 7 μL of distilled water. The reaction mixture was then incubated at 65°C (5 min) for denaturation, chilled on ice for 1 min and added 4 μL of 5×RT buffer (Life Technologies), 1 μL of 0.1 M dithiothreitol (DTT), 1 μL of the RNase out (Life Technologies) and 1 μL of Superscript III Reverse Transcriptase (Life Technologies). After the addition of these reagents, the reaction mixture was incubated at 50°C (1 h) for random primer annealing and 70°C (15 min) for cDNA preparation. One microliter of the reaction mixture was then used for PCR. The genomic DNA was isolated from MEF cells that were derived from hTRB3 and wild mice. The primer sequences of PCR analysis used in this study were as follows: human TRB3-specific primer set, hTRB3F (5′-CAA GTC GCT CTG AAG GTT CC-3′) and hTRB3R (5′-CCA TCC TAC TCT GGC AAA GC-3′), Cre/loxP recombination primer set, CAGpF (5′-CGT GCT GGT TGT TGT GCT GTC T-3′), and geno-hTRB3R (5′-ATC CGT CGA CCC TTG TCA TC-3′). β-Actin-specific DNA fragments from the same RNA samples were amplified and served as internal controls. Primers actin F (5′-CCG TAA AGA CCT CTA TGC CAA CA-3′) and actin R (5′-CGG ACT CAT CGT ACT CCT GCT T-3′) were used for amplification of β-actin. Interleukin-2 (IL-2)-specific DNA fragments from genomic DNA samples were also amplified and served as internal controls. Primers IL-2 F (5′-CTA GGC CAC AGA ATT GAA AGA TCT-3′) and IL-2 R (5′-GTA GGT GGA AAT TCT AGC ATC ATC C-3′) were used for amplification of IL-2. PCR was conducted for 26–30 cycles in an iCycler (Bio-Rad Laboratories, Inc., Hercules, CA, U.S.A.). Each amplification cycle consisted of at 94°C (0.5 min) for denaturation, 60°C (0.5 min) for primer annealing, and 72°C (1 min) for extension. After PCR amplification, the DNA fragments were stained with ethidium bromide and analyzed by 2% agarose gel electrophoresis. The results were confirmed by repeating experiments.

Western Blot Assays These assays were done with established procedures.[19] The cells were lysed in radioimmunoprecipitation assay (RIPA) buffer (50 mM Tris–HCl (pH 8.0), 150 mM NaCl, 0.1% sodium dodecyl sulfate (SDS), 0.5% deoxycholate, and 1% Triton X-100). The lysates were subjected to SDS-polyacrylamide gel electrophoresis (PAGE) (12.5%), transferred onto a polyvinylidene difluoride (PVDF) membrane (Immobilon P, Millipore Corp., Bedford, MA, U.S.A.) and probed with the antibodies. The primary antibodies used in the present study were anti-β-actin monoclonal antibody (AC-15, Sigma, St. Louis, MO, U.S.A.) and anti-FLAG monoclonal antibody (M2, Sigma, St. Louis, MO, U.S.A.). The antiserum against human TRB3 was prepared as described previously.[7] Proteins of interest were visualized using immunoStar Zeta (Wako) and light emission was quantified with a Light-capture (ATTO Corp., Tokyo, Japan). Each assay was repeated more than three times to confirm the results.

Statistical Analysis Differences in the mean diameter of the nucleus of the liver cells between hTRB3 and wild type mice were analyzed by Student's or Welch's *t*-test. The value of $p<0.05$ was considered to be significant.

RESULTS AND DISCUSSION

We have developed a novel variation of the transgenic mouse model by using Cre/loxP system to express TRB3 protein in the liver, spleen, and kidney tissues. Mean diameter of nucleus was greater in hepatic cells transfected with hTRB3 than non-transfected hepatocytes. This morphological difference depending on transfection status is in accordance with our recent experiments demonstrating that hTRB3 transfected mouse mammary tumor cells exhibited enlarged nuclear size and that *TRB3* gene promotes cell proliferation and chromosomal instability by causing polyproidization during development of mouse mammary tumor.[14] Taken together, *hTRB3* gene may influence its response to morphological function and the present animal model system would be useful to see if this gene causes *de novo* morphological changes leading to tumorigenesis in a specific organ site.

Conditional Expression of Human TRB3 (hTRB3) Transgene Was Controlled by Cre-Recombinase The system was originated by investigators.[15,20] This system is a powerful on/off switching tool when timed/tissue specific expression of gene is critical in cultured cells or transgenic animals. This system can also be used in experiments of developmental processes involving proteins that are suspected of exerting different functions in embryogenesis and in adult animals and that are lethal if the gene is expressed in the embryo. In the present study, little was known about the lethality when hTRB3 gene was introduced into mouse embryo. Thus, we selected this Cre/loxP system to avoid the issue of embryonic lethal.

In Fig. 2 panel A, lysate sample in lane 1 was derived from COS7 cells that were transfected with both hTRB3 transgene construct (pCALNL-flag-hTRB3) and Cre expression vector (pxCANCre). Lysate samples of lanes 4 and 5 were negative and positive controls, respectively. When COS7 cell were transfected with both hTRB3 transgene construct and Cre expression vector, the FLAG expression was present (lane 1) as seen in the positive control (lane 5). Negative and positive controls (lanes 4 and 5) consisted of COS7 cells transfected with empty vector (pCALNL5) and hTRB3 expression vector (pcDNA3.1-flag-hTRB3), respectively. These findings indicate that expression of hTRB3 transgene was controlled by the Cre/loxP system. This hTRB3 construct was used for injection as described below.

Generation of hTRB3 Transgenic Mouse Wagner *et al.* previously reported that the ratio of the number of offspring/embryos to foster mother was 23%.[21] The ratio of the number of mouse that expresses transgene/the number of offspring was 10–40%.[22]

In the present Cre/loxP system, the ratio of the number of mouse expressing transgene/embryos to foster mother was 4/184=2%. After infection of Cre, this enzyme excises the stuffer DNA region loxP–*neo*-poly A–loxP (Fig. 1). This step initiates gene expression of hTRB3. By introducing hTRB3 transgene construct (Fig. 1) into pronuclei of mouse embryo, four hTRB3 mice were eventually obtained (Fig. 2 panel B). These four hTRB3 mice were mated with wild mice and offspring were produced. hTRB3 genotyping was done using genomic DNA derived from the offspring, and most of them carried hTRB3 (Fig. 2 panel C). In three of four mice, hTRB3 gene was transmitted to next generation.

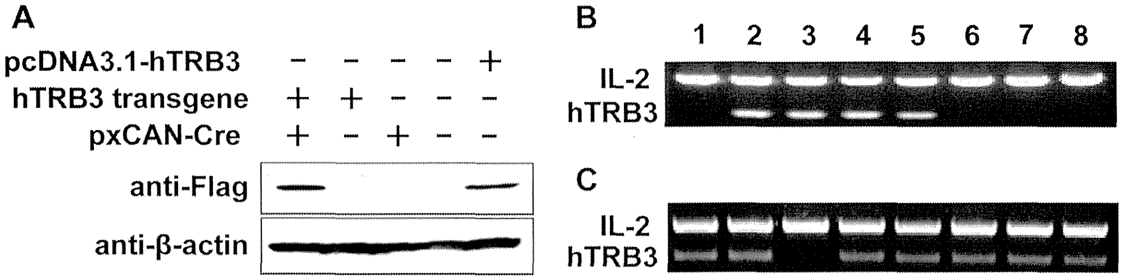

Fig. 2. Confirmation of hTRB3 Protein Expression and Detection of hTRB3 DNA Fragment

(A) Conditional expression of hTRB3. Lysate sample in lane 1 was derived from COS7 cells that were transfected with both hTRB3 construct (pCALNL-flag-hTRB3) and Cre expression vector (pxCANCre). Lysate samples of lanes 2 and 3 consisted of COS7 cells transfected with hTRB3 construct and Cre expression vector, respectively. Lysate samples of lanes 4 and 5 were negative and positive controls, respectively. Negative and positive controls (lanes 4 and 5) consisted of COS7 cells transfected with empty vector (pCALNL5) and hTRB3 expression vector (pcDNA3.1-flag-hTRB3), respectively. The FLAG expression was present (lane 1) as seen in the positive control (lane 5). (B, C) Detection of hTRB3 DNA fragments by PCR assay. We used hTRB3 transgenic mice (hTRB3 mice) as described in Materials and Methods. Genomic DNA was extracted from mice tails and used for amplification of hTRB3 and IL-2 DNA fragments. (B) hTRB3 DNA fragment was seen in 4 mice of 8 potential transgenic mice. The number indicates the individual mouse number. (C) hTRB3 DNA fragment was seen in 7 of 8 offspring generated by mating hTRB3 mice with wild mice.

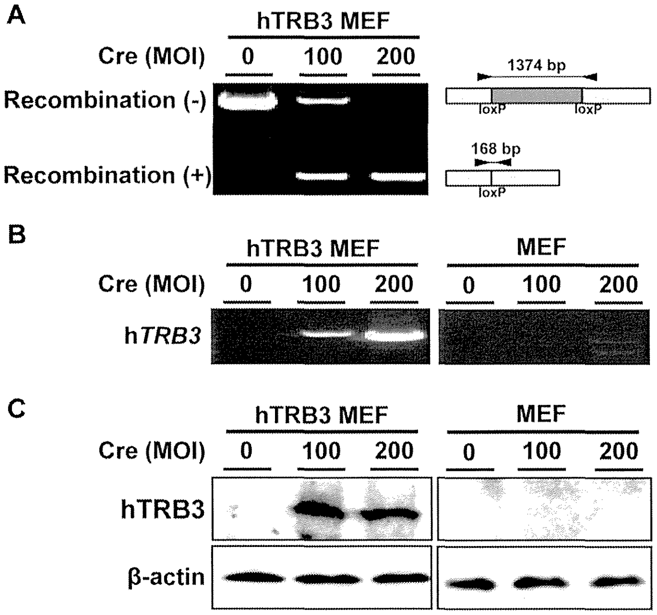

Fig. 3. Confirmation of Recombination of hTRB3 Construct and hTRB3 mRNA/Protein Expression in hTRB3 MEF Cells

hTRB3 MEF and MEF cells were generated from hTRB3 and wild mice, respectivly. These cells were treated with Cre expressing adenovirus (0, 100, 200 MOI). MOI indicates multiplicity of infection. (A) Confirmation of recombination of hTRB3 construct in hTRB3 MEF cells by PCR assay. A 168-bp DNA fragment derived from recombinant hTRB3 construct was seen in cells treated with Cre expressing adenovirus. hTRB3 DNA fragments were not PCR-amplified in MEF cells (data not shown). (B) Confirmation of hTRB3 mRNA expression in hTRB3 MEF/MEF cells by RT-PCR assay. Increasing mRNA expression was seen in hTRB3 MEF cells (left panel). No mRNA expression was seen in MEF cells (right panel). (C) Confirmation of hTRB3 protein expression by Western blot assay. hTRB3 protein expression was observed in hTRB3 MEF cells but not in MEF cells. β-Actin was used as an internal control.

To confirm whether Cre-mediated recombination of the transgene occurs in MEF cells, we examined the existence of DNA fragment consisting of hTRB3 construct by PCR assay. hTRB3 MEF cells and MEF cells were generated from 14-d-old embryos of hTRB3 and wild mice, respectively. Cells were then infected with Cre expressing adenovirus as described in Materials and Methods. A 168-bp DNA fragment was seen when the recombination occurred (Fig. 3 panel A). However, a longer 1374-bp DNA fragment was seen unless hTRB3 MEF cells were treated with Cre expressing adenovirus, indicating no recombination of the transgene. We also examined the mRNA/protein expression status of hTRB3 by RT-PCR/Western blot assays. There was a marked mRNA/protein expression of hTRB3 in hTRB3 MEF cells treated with Cre (Fig. 3, panels B left and C left). There was no expression seen in MEF cells that were treated with Cre (Fig. 3, panels B right and C right).

hTRB3 Protein Is Expressed in Liver, Spleen and Kidney Tissues, and hTRB3 Gene Affects the Nuclear Size in the Liver Cell To examine whether *hTRB3* gene causes *de novo* morphological changes leading to tumorigenesis in a specific organ site, we performed immunohistochemical analysis and hematoxylin/eosin staining for histopathological examination in liver, spleen, and kidneys of the hTRB3 mouse. There were no apparent abnormalities seen in morphology and behavior in either hTRB3 or wild mice. As shown in Fig. 4, hTRB3 and wild mice, both of which were not infected with Cre expressing adenovirus, exhibited no significant histopathological differences in the liver (Figs. 4A, D), spleen (Figs. 4B, E), and kidney (Figs. 4C, F) tissues. There were also no apparent histopathological differences in the spleen and kidney tissues between hTRB3 and wild mice, both of which were infected with Cre expressing adenovirus (Figs. 5B, E, and Figs. 5C, F). In the hTRB3 mouse that infected with Cre expressing adenovirus, approximately 20% of hepatocyets exhibited positive cytoplasmic staining of FLAG, indicating hTRB3 protein was expressed in these hepatocytes (Fig. 6A, arrow), whereas the remaining 80% stained faintly or uncertainly. Positive FLAG staining was also seen in sinusoid in liver tissue (Fig. 6A arrowhead). In the spleen of the hTRB3 mice, approximately 10% of lymphocytes were positively stained with FLAG (Fig. 6B). In the kidney of the hTRB3 mice, approximately 20% of epithelial cells of the tubules and collecting duct were positively stained with FLAG (Fig. 6C). Also, endothelial cells of capillaries of glomeruli were positive (Fig. 6D). Perivascular inflammation in liver tissue was also seen in the hTRB3 mouse (Fig. 5A). In liver cells of the hTRB3 mouse, the mean longest diameter of nucleus was significantly greater than that of the wild mice (9.4 ± 0.19 *versus* $6.3\pm0.11\,\mu$m, $p<0.001$) (Fig. 5A *versus* 5D). These results indicate that the Cre/loxP recombination system functions at least in part in liver, spleen, and kidney of the C57BL/6NCrSlc mouse, and that hTRB3 gene causes morphological changes in nuclear size of hepatocytes. An increase in nuclear size occurred in both FLAG-positive

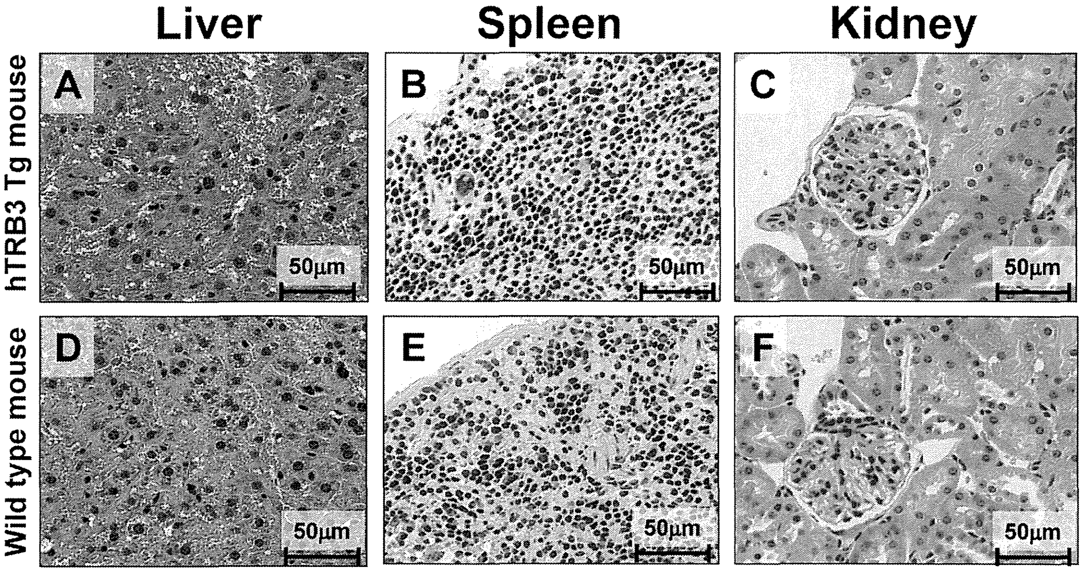

Fig. 4. Representative Histological Features of the Liver, Spleen, and Kidney Tissues of hTRB3 and Wild Mice without Cre Treatment

Note that no apparent histological differences were observed between hTRB3 (A–C) and wild (D–F) mice, both of which were not introduced hTRB3 transgene. Magnification was ×400 in all six images.

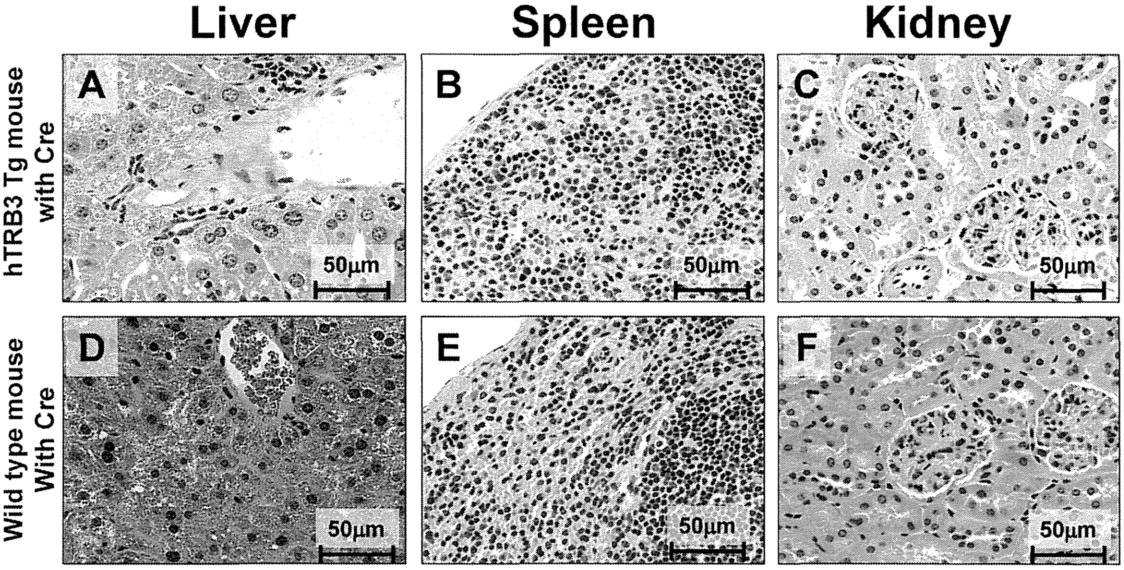

Fig. 5. Representative Histological Features of the Liver, Spleen, and Kidney Tissues of hTRB3 and Wild Mice with Cre Treatment

hTRB3 and wild mice were infected with Cre expressing adenovirus and HE staining was conducted with liver, spleen and kidney tissues derived from hTRB3 mouse (A–C) or wild mouse (D–F). No apparent abnormality was seen in liver tissue derived from wild mouse (B). Note that nuclear size of hepatocyte in the liver tissue derived from hTRB3 mouse increases compared to that of wild mouse (A). Slight perivascular inflammation is also seen (A). Note that no apparent histological differences in spleen or kidney tissues were observed between hTRB3 (B, C) and wild (E, F) mice. Magnification was ×400 in all six images.

and negative hepatocytes (Figs. 5A, D). This is presumably because endogenous TRB3 in mouse hepatocytes may function as exogenous hTRB3 simultaneously does. Indeed, in a recent experiment we found that both endogenous and exogenous TRB3 express in a cell line that stably expresses exogenous TRB3 gene.[14] Further, Bowers *et al.* postulate that there is a feedback response of TRB3 protein accumulation activating a higher expression of TRB3 transcript.[3]

We first estimated that Cre-mediated recombination of the transgene had occurred more than 50% in frequency. Anton *et al.* also estimated approximately 50% of Cre-dependent recombination *in vitro*.[20] Kudoh *et al.* developed a mouse model for Duchenne muscular dystrophy using a Cre/loxP recombination system, and the ratio of the number of 100% chimeras/the number of embryo transplanted ranged from zero to 5%.[23] In our experiment, actual efficiency of the present system resulted in 20%. Differences in experimental systems (*i.e.*, *in vitro*/*in vivo*, animal strain used in the experiment, sequence of the restrictive target sites, and MOI) may explain discrepancies reported on efficiency of recombination. It may be possible for us to improve on this efficiency by optimizing MOI values or the timing of adenovirus infection.

Commonly used adenoviruses derived from human serotype 2 (Ad2) and 5 (Ad5) infect a broad range of organ tissues through interaction with the 46-kDa coxackie and adenovirus receptor (CAR).[24] The major issue for successful site specific transgene delivery is tissue selectivity. Systemically injected adenovirus into mice primarily localize to hepatocytes with

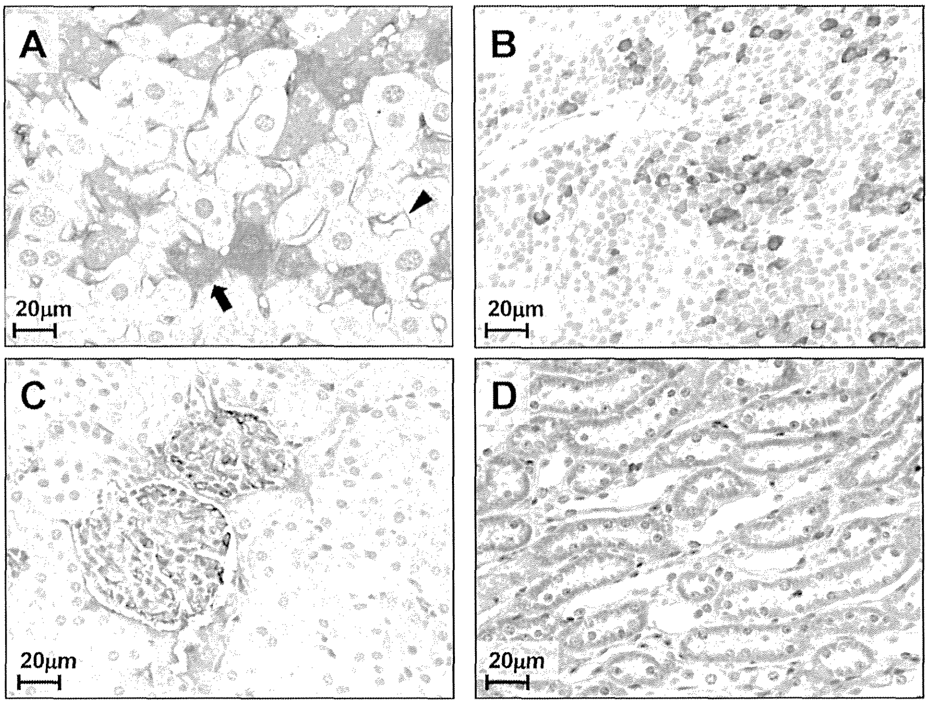

Fig. 6. Representative Immunohistochemical Analysis of Liver, Spleen and Kidney Tissues of hTRB3 and Wild Mice with Cre Treatment

hTRB3 and wild mice were infected with Cre expressing adenovirus and immunohistochemical staining of liver (A), spleen (B) and kidney (C, D) tissues derived from hTRB3 mouse were done. (A) Immunohistochemical staining of liver tissue derived from hTRB3 mouse. Note that FLAG-mediated hTRB3 protein expression was seen in the cytoplasmic region of hepatocytes (arrow) and sinusoid of the liver tissue (arrowhead). FLAG-mediated hTRB3 protein expression was faintly or uncertainly stained in the remaining hepatocytes. (B) FLAG-mediated hTRB3 protein expression was seen in lymphocytes of spleen tissue. (C) In the kidney tissue of the hTRB3 mouse, hTRB3 was positively stained in epithelial cells of the tubules and collecting duct. (D) hTRB3 was also positively stained in endothelial cells of the capillary of glomeruli of the kidney. Magnification was ×400 in all six images.

consequent hepatotoxicity.24–26) In the present study, we used adenovirus vector Ad5 and FLAG-mediated expression of hTRB3 transgene was seen in three organs such as liver, spleen, and kidneys, indicating low tissue selectivity.

In the hTRB3 mice, we found that nuclear diameter of FLAG-stained hepatocytes was significantly greater than that of wild mice. Some investigators report an increase in nuclear size as the disorder progresses from normal to carcinoma.27,28) Furthermore, nuclear size increases monotonically with nuclear DNA content.29) The findings in the present study together with our recent experiment14) indicate that TRB3 affects nuclear size of hepatocytes that were infected with Ad5. There are several documents demonstrating morphological changes and hepatocarcinogenesis. Large cell change of hepatocytes was regarded as a precancerous lesion.30) Nuclear enlargement of hepatocytes was induced by the treatment of animals with carcinogen.31–33) Of these reports, Clawson *et al.* found that hepatocarcinogen induced nuclear enlargement is associated with substantial diploid to tetraploid shifts in hepatocytes.31) Regarding TRB3's function, it is reported that TRB3 accumulates in response to fasting and inhibits the activation of the kinase Akt in the liver.1,34) TRB3 also stimulates lipolysis by triggering the degradation of acetyl-coenzyme A carboxylase (ACC) in adipose tissue.10)

Acknowledgments We thank Tomomi Miyamoto for excellent technical support on the production of transgenic mice. This study was supported by Grants-in-Aid from the Ministry of Education, Culture, Sports, Science and Technology of Japan and the Ministry of Health, Labour, and Welfare of Japan.

REFERENCES

1) Du K, Herzig S, Kulkarni RN, Montminy M. TRB3: a tribbles homolog that inhibits Akt/PKB activation by insulin in liver. *Science*, **300**, 1574–1577 (2003).
2) Wilkin F, Suarez-Huerta N, Robaye B, Peetermans J, Libert F, Dumont JE, Maenhaut C. Characterization of a phosphoprotein whose mRNA is regulated by the mitogenic pathways in dog thyroid cells. *Eur. J. Biochem.*, **248**, 660–668 (1997).
3) Bowers AJ, Scully S, Boylan JF. SKIP3, a novel *Drosophila* tribbles ortholog, is overexpressed in human tumors and is regulated by hypoxia. *Oncogene*, **22**, 2823–2835 (2003).
4) Kato S, Du K. TRB3 modulates C2C12 differentiation by interfering with Akt activation. *Biochem. Biophys. Res. Commun.*, **353**, 933–938 (2007).
5) Kiss-Toth E, Bagstaff SM, Sung HY, Jozsa V, Dempsey C, Caunt JC, Oxley KM, Wyllie DH, Polgar T, Harte M, O'neill LAJ, Qwamstrom EE, Dower SK. Human tribbles, a protein family controlling mitogen-activated protein kinase cascades. *J. Biol. Chem.*, **279**, 42703–42708 (2004).
6) Örd D, Ord T. Mouse NIPK interacts with ATF4 and affects its transcriptional activity. *Exp. Cell Res.*, **286**, 308–320 (2003).
7) Ohoka N, Yoshii S, Hattori T, Onozaki K, Hayashi H. TRB3, a novel ER stress-inducible gene, is induced *via* ATF4-CHOP pathway and is involved in cell death. *EMBO J.*, **24**, 1243–1255 (2005).
8) Bezy O, Vernochet C, Gesta S, Farmer SR, Kahn CR. TRB3 blocks adipocyte differentiation through the inhibition of C/EBPbeta transcriptional activity. *Mol. Cell. Biol.*, **27**, 6818–6831 (2007).
9) Takahashi Y, Ohoka N, Hayashi H, Sato R. TRB3 suppresses adipocyte differentiation by negatively regulating PPARgamma transcriptional acltivity. *J. Lipid Res.*, **49**, 880–892 (2008).
10) Qi L, Heredia JE, Altarejos JY, Screaton R, Goebel N, Niessen S, Macleod IX, Liew CW, Kulkami RN, Bain J, Newgard C, Nelson

M, Evans RM, Yates J, Montminy M. TRB3 links the E3 ubiquitin ligase COP1 to lipid metabolism. *Science*, **312**, 1763–1766 (2006).

11) Jin G, Yamazaki Y, Takuwa M, Takahara T, Kaneko K, Kuwata T, Miyata S, Nakamura T. Trib1 and Evi1 cooperate with Hoxa and Meis1 in myeloid leukemogenesis. *Blood*, **109**, 3998–4005 (2007).

12) Dedhia PH, Keeshan K, Uljon S, Xu L, Vega ME, Shestova O, Zaks-Zilberman M, Romany C, Blacklow SC, Pear WS. Differential ability of Tribbles family members to promote degradation of C/EBPalpha and induce acute myelogenous leukemia. *Blood*, **116**, 1321–1328 (2010).

13) Xu J, Lv S, Qin Y, Shu F, Xu Y, Chen J, Xu BE, Sun X, Wu J. TRB3 interacts with CtIP and is overexpressed in certain cancers. *Biochim. Biophys. Acta*, **1770**, 273–278 (2007).

14) Sakai Y, Fukamachi K, Futakuchi M, Hayashi H, Suzui M. Promotive effects of cell proliferation and chromosomal instability induced by tribbles-related protein 3 in mouse mammary tumor cells. *Oncol. Rep.*, **30**, 64–70 (2013).

15) Kanegae Y, Lee G, Sato Y, Tanaka M, Nakai M, Sakaki T, Sugano S, Saito I. Efficient gene activation in mammalian cells by using recombinant adenovirus expressing site-specific Cre recombinase. *Nucleic Acids Res.*, **23**, 3816–3821 (1995).

16) Tanaka H, Fukamachi K, Futakuchi M, Alexander DB, Long N, Tamamushi S, Minami K, Seino S, Ohara H, Joh T, Tsuda H. Mature acinar cells are refractory to carcinoma development by targeted activation of Ras oncogene in adult rats. *Cancer Sci.*, **101**, 341–346 (2010).

17) Niwa H, Yamamura K, Miyazaki J. Efficient selection for high-expression transfectants with a novel eukaryotic vector. *Gene*, **108**, 193–199 (1991).

18) Suzui M, Inamine M, Kaneshiro T, Morioka T, Yoshimi N, Suzuki R, Kohno H, Tanaka T. Indole-3-carbinol inhibits the growth of human colon carcinoma cells but enhances the tumor multiplicity and volume of azoxymethane-induced rat colon carcinogenesis. *Int. J. Oncol.*, **27**, 1391–1399 (2005).

19) Suzui M, Masuda M, Lim JT, Albanese C, Pestell RG, Weinstein IB. Growth inhibition of human hepatoma cells by acyclic retinoid is associated with induction of p21(CIP1) and inhibition of expression of cyclin D1. *Cancer Res.*, **62**, 3997–4006 (2002).

20) Anton M, Graham FL. Site-specific recombination mediated by an adenovirus vector expressing the Cre recombinase protein: a molecular switch for control of gene expression. *J. Virol.*, **69**, 4600–4606 (1995).

21) Wagner TE, Hoppe PC, Jollick JD, Scholl DR, Hodinka RL, Gault JB. Microinjection of a rabbit beta-globin gene into zygotes and its subsequent expression in adult mice and their offspring. *Proc. Natl. Acad. Sci. U.S.A.*, **78**, 6376–6380 (1981).

22) Hogan B, Beddington R, Costantini F, Lacy E. *Manipulating the mouse embryo: a laboratory manual.* 2nd ed. (Hogan BL ed.) CSHL Press, New York, p. 220 (1994).

23) Kudoh H, Ikeda H, Kakitani M, Ueda A, Hayasaka M, Tomizuka K, Hanaoka K. A new model mouse for Duchenne muscular dystrophy produced by 2.4 Mb deletion of dystrophin gene using Cre-loxP recombination system. *Biochem. Biophys. Res. Commun.*, **328**, 507–516 (2005).

24) Law LK, Davidson BL. What does it take to bind CAR? *Mol. Ther.*, **12**, 599–609 (2005).

25) Huard J, Lochmüller H, Acsadi G, Jani A, Massie B, Karpati G. The route of administration is a major determinant of the transduction efficiency of rat tissues by adenoviral recombinants. *Gene Ther.*, **2**, 107–115 (1995).

26) Wood M, Perrotte P, Onishi E, Harper ME, Dinney C, Pagliaro L, Wilson DR. Biodistribution of an adenoviral vector carrying the luciferase reporter gene following intravesical or intravenous administration to a mouse. *Cancer Gene Ther.*, **6**, 367–372 (1999).

27) Boon ME, Kurver PJ, Baak JP, Thompson HT. The application of morphometry in gastric cytological diagnosis. *Virchows Arch. A Pathol. Anat. Histol.*, **393**, 159–164 (1981).

28) Boysen M, Reith A. Discrimination of various epithelia by simple morphometric evaluation of the basal cell layer. A light microscopic analysis of pseudostratified, metaplastic and dysplastic nasal epithelium in nickel workers. *Virchows Arch. B Cell Pathol. Incl. Mol. Pathol.*, **42**, 173–184 (1983).

29) Danielsen H, Lindmo T, Reith A. A method for determining ploidy distributions in liver tissue by stereological analysis of nuclear size calibrated by flow cytometric DNA analysis. *Cytometry*, **7**, 475–480 (1986).

30) Anthony PP, Vogel CL, Barker LF. Liver cell dysplasia: a premalignant condition. *J. Clin. Pathol.*, **26**, 217–223 (1973).

31) Clawson GA, Moody DE, James J, Smuckler EA. Nuclear envelope alterations accompanying thioacetamide-related enlargement of the nucleus. *Cancer Res.*, **41**, 519–526 (1981).

32) Enzmann H, Kühlem C, Löser E, Bannasch P. Dose dependence of diethylnitrosamine-induced nuclear enlargement in embryonal turkey liver. *Carcinogenesis*, **16**, 1351–1355 (1995).

33) Wiemann C, Enzmann H, Löser E, Schlüter G. Nonlinearity of nuclear enlargement in hepatocytes induced by the carcinogen *N'*-nitrosomorpholine *in vivo*. *Cancer Detect. Prev.*, **23**, 485–495 (1999).

34) Koo SH, Satoh H, Herzig S, Lee CH, Hedrick S, Kulkarni R, Evans RM, Olefsky J, Montminy M. PGC-1 promotes insulin resistance in liver through PPARalpha-dependent induction of TRB-3. *Nat. Med.*, **10**, 530–534 (2004).

RESEARCH ARTICLE

Comparative Study of Toxic Effects of Anatase and Rutile Type Nanosized Titanium Dioxide Particles *in vivo* and *in vitro*

Takamasa Numano[1,3], Jiegou Xu[2], Mitsuru Futakuchi[1], Katsumi Fukamachi[1], David B Alexander[2], Fumio Furukawa[3], Jun Kanno[4], Akihiko Hirose[4], Hiroyuki Tsuda[2], Masumi Suzui[1]*

Abstract

Two types of nanosized titanium dioxide, anatase (anTiO_2) and rutile (rnTiO_2), are widely used in industry, commercial products and biosystems. TiO_2 has been evaluated as a Group 2B carcinogen. Previous reports indicated that anTiO_2 is less toxic than rnTiO_2, however, under ultraviolet irradiation anTiO_2 is more toxic than rnTiO_2 *in vitro* because of differences in their crystal structures. In the present study, we compared the *in vivo* and *in vitro* toxic effects induced by anTiO_2 and rnTiO_2. Female SD rats were treated with 500 μg/ml of anTiO_2 or rnTiO_2 suspensions by intra-pulmonary spraying 8 times over a two week period. In the lung, treatment with anTiO_2 or rnTiO_2 increased alveolar macrophage numbers and levels of 8-hydroxydeoxyguanosine (8-OHdG); these increases tended to be lower in the anTiO_2 treated group compared to the rnTiO_2 treated group. Expression of MIP1α mRNA and protein in lung tissues treated with anTiO_2 and rnTiO_2 was also significantly up-regulated, with MIP1α mRNA and protein expression significantly lower in the anTiO_2 group than in the rnTiO_2 group. In cell culture of primary alveolar macrophages (PAM) treated with anTiO_2 and rnTiO_2, expression of MIP1α mRNA in the PAM and protein in the culture media was significantly higher than in control cultures. Similarly to the *in vivo* results, MIP1α mRNA and protein expression was significantly lower in the anTiO_2 treated cultures compared to the rnTiO_2 treated cultures. Furthermore, conditioned cell culture media from PAM cultures treated with anTiO_2 had less effect on A549 cell proliferation compared to conditioned media from cultures treated with rnTiO_2. However, no significant difference was found in the toxicological effects on cell viability of ultra violet irradiated anTiO_2 and rnTiO_2. In conclusion, our results indicate that anTiO_2 is less potent in induction of alveolar macrophage infiltration, 8-OHdG and MIP1α expression in the lung, and growth stimulation of A549 cells *in vitro* than rnTiO_2.

Keywords: Nanosized titanium dioxide - anatase - rutile - lung toxicity - MIP1α

Asian Pac J Cancer Prev, **15 (2)**, 929-935

Introduction

There are three mineral forms of natural titanium dioxide particles: rutile, anatase and brookite. Engineered anatase and rutile nanosized titanium dioxide particles (anTiO_2 and rnTiO_2) are being manufactured in large quantities worldwide and applied in many fields including material industry, electronic industry, commercial products and biosystems. Due to differences in crystal structure, anTiO_2 has better photocatalytic activity than rnTiO_2 (Kakinoki et al., 2004). Accordingly, anTiO_2 is mainly used in paints, such as surface painting of the walls and windows of buildings and vehicles, and photocatalytic systems, while rnTiO_2 is preferentially used in cosmetics, sunscreen and food additives.

Large quantity production and widespread application of nTiO_2 have given rise to concern about its health and environmental effects. Anatase and rutile type titanium dioxide particles, nanosized and larger, are evaluated as Group 2B carcinogens (possibly carcinogenic to humans) by WHO/International Agency for Research on Cancer (IARC, 2010), based on 2-year animal aerosol inhalation studies (Mohr et al., 2006). Pulmonary exposure to rnTiO_2 promotes DHPN-induced lung carcinogenesis in rats, and the promotion effect is possibly associated with rnTiO_2 burdened alveolar macrophage derived macrophage inflammatory protein 1 alpha (MIP1α), which acts as a growth factor to stimulate the proliferation of human lung adenocarcinoma cells (A549) *in vitro* (Xu et al., 2010). Dermal application of anTiO_2 has been shown to cause significant increases in the level of superoxide dismutase and malondialdehyde in hairless mice (Wu et al., 2009).

Size and photoactivation affect the *in vitro* toxicity of anTiO_2 and rnTiO_2. anTiO_2 (10 and 20 nm) induces

[1]*Department of Molecular Toxicology, Nagoya City University Graduate School of Medical Sciences and Medical School,* [2]*Laboratory of Nanotoxicology Project, Nagoya City University, Nagoya,* [3]*DIMS Institute of Medical Science, Aichi,* [4]*National Institute of Health Sciences, Tokyo, Japan *For correspondence: suzui@med.nagoya-cu.ac.jp*

oxidative DNA damage, lipid peroxidation and micronuclei formation, and increases hydrogen peroxide and nitric oxide production in BEAS-2B cells, a human bronchial epithelial cell line, but anTiO_2 200 nm particles do not (Gurr et al., 2005). In contrast, both nano-sized and 200nm ruTiO_2 are toxic *in vitro* (Gurr et al., 2005; Sayes et al., 2006). On the other hand, under ultraviolet irradiation, anTiO_2 is 100 times more toxic to human dermal fibroblasts and A549 cells than rnTiO_2, and is more potent than rnTiO_2 in the induction of lactate dehydrogenase release, reactive oxygen species production and interleukin 8 secretion (Sayes et al., 2006). Experimental data demonstrating differences in the toxic effects of anTiO_2 and rnTiO_2 *in vivo*, however, are still lacking.

Respiratory exposure to nTiO_2 particles can occur both at the workplace, e.g., in manufacturing and packing sites, and outside the workplace during their use (Maynard et al., 2006; Schulte et al., 2008). In the present study, we delivered anTiO_2 and rnTiO_2 to the rat lung by trans-tracheal intra-pulmonary spraying (TIPS) and compared lung inflammation and several toxicological parameters induced by anTiO_2 and rnTiO_2. The results indicated that obvious lung inflammatory lesions were not observed in the rats, and anTiO_2 or rnTiO_2 particles were phagocytosed by alveolar macrophages. Analysis of alveolar macrophage induction, 8-OHdG level in the lung, and MIP1α expression both *in vivo* in the lung and *in vitro* in PAM indicated that anTiO_2 elicited lower levels of biological responses than rnTiO_2. Long-term toxic effects of anTiO_2 and rnTiO_2 still need to be clarified.

Materials and Methods

Preparation and characterization of nTiO_2 suspension

Nanosized TiO_2 particles (anatase type without coating, primary size 25 nm and rutile type without coating, primary size 20 nm) were provided by Japan Cosmetic Association, Tokyo, Japan. Both anTiO_2 and rnTiO_2 particles were suspended in saline at 500 μg/ml and then autoclaved. The suspensions were sonicated for 20 min shortly before use to prevent aggregate formation.

Characterization of nTiO_2 was conducted as follows: The shapes of nTiO_2 in suspension were imaged by transmission electron microscopy (TEM) and scanning electron microscopy (SEM). Element analysis was performed by a an X-ray microanalyzer (EDAX, Tokyo, Japan), after aliquots of nTiO_2 were loaded onto a carbon sheet. For size distribution analysis, aliquots of the 500 μg/ml nTiO_2 suspension were loaded onto clean glass slides and photographed under a polarized light microscope (Olympus BX51N-31P-O polarized light microscope, Tokyo, Japan), and the photos were then analyzed by an image analyzer system (IPAP, Sumika Technos Corporation, Osaka, Japan). Over 1000 particles of anTiO_2 and rnTiO_2 were measured.

Animals

Female Sprague-Dawley rats (SD rats) were purchased from CLEA Japan Co., Ltd (Tokyo, Japan). The animals were housed in the animal center of Nagoya City University Medical School, maintained on a 12 hour light-dark cycle and received oriental MF basal diet (Oriental Yeast Co., Tokyo, Japan) and water *ad lib*. The research was conducted according to the Guidelines for the Care and Use of Laboratory Animals of Nagoya City University Medical School and the experimental protocol was approved by the Institutional Animal Care and Use Committee (H22M-19).

Trans-tracheal intra-pulmonary spraying (TIPS) protocol

Three groups of 6 female SD rats (Group 1, saline; Group 2, anTiO_2; and Group 3, rnTiO_2) aged 9 weeks were acclimated for 7 days prior to the start of the study. Saline and nTiO_2 suspensions were administered by TIPS to the animals under isoflurane anesthesia: The nozzle of a Microsprayer (series IA-1B Intratracheal Aerosolizer, Penn-century, Philadelphia, PA) connected to a 1 ml syringe was inserted into the trachea through the larynx and a total volume of 0.5 ml suspension was sprayed into the lungs synchronizing with spontaneous inspiration by the animal (Xu et al., 2010). Rats were treated once every the other day over a 2 week period, a total of eight treatments. The total amount of an$TiO_2$and rnTiO_2 administered to Groups 2 and 3 was 2.0 mg per rat. Six hours after the last spraying, the animals were killed and the whole lung was excised and divided into two parts; the left lung was cut into pieces and immediately frozen at -80°C and used for biochemical analysis, and the right lung was fixed in 4% paraformaldehyde solution in phosphate-buffered saline (PBS) adjusted to pH 7.3 and processed for immunohistochemical, light microscopic and transmission electron microscopic (TEM) examinations.

Light microscopy and transmission electron microscopy

Hematoxylin and eosin (H&E) stained sections were used for pathological observation. The number of alveolar macrophages in H&E lung tissue slides was counted and expressed as number per mm^2.

Slides were observed under light microscopic observation, the corresponding area in the paraffin block was cut out, deparaffinized and embedded in epoxy resin and processed for TEM and titanium element analysis with a JEM-1010 transmission electron microscope (JEOL Co. Ltd, Tokyo, Japan) equipped with an X-ray microanalyzer (EDAX, Tokyo, Japan).

Analysis of 8-hydroxydeoxy guanosine levels

For the analysis of 8-hydroxydeoxyguanosine (8-OHdG) levels, genomic DNA was isolated from a piece of the left lung with a DNA Extractor WB kit (Wako Chemicals Co. Ltd). 8-OHdG levels were determined with an 8-OHdG ELISA Check kit (Japan Institute for Control of Aging, Shizuoka, Japan).

RNA isolation, cDNA synthesis and RT-PCR analysis of gene expression

Pieces of the left lungs (50-100 mg) were thawed, rinsed 3 times with ice cold PBS, and total RNA was isolated using 1 ml Trizol Reagent (Invitrogen, Karlsruhe, Germany). For reverse transcription PCR (RT-PCR) and real-time PCR, first strand cDNA synthesis from 2 mg of total RNA was performed using SuperScript™ III First-Strand Synthesis